Solvent-Induced Nanoscopic Surface Morphology on Polymer Thin Films

by

Tiana Trumpour

A thesis
presented to the University of Waterloo
in fulfillment of the
thesis requirement for the degree of
Masters of Science
in
Physics (Nanotechnology)

Waterloo, Ontario, Canada, 2020

Author's Declaration

I hereby declare that I am the sole author of this thesis. This is a true copy of the thesis, including any required final revisions, as accepted by my examiners.

I understand that my thesis may be made electronically available to the public.

Abstract

Polymer thin films are studied extensively due to their important applications in the fields of material coatings, biomedical devices, nanoelectronics, and more. Many of these applications directly depend on the surface properties of the films as this may influence the efficacy or properties of the resultant mechanism. The usual methods to create and use thin films involve the application of solvents to the surface. Processes such as nanolithography apply solvents of a poor quality to the thin films as a form of washing, with the expectation that no lasting effects will be present on the surface. However, this thesis proves that a nanoscopic morphology is resultant from the application of poor solvents to the surface of polymer thin films. It has been shown that the morphology exhibits a characteristic length scale which is independent of the poor solvent used and independent of molecular weight at large chain lengths. Finally, a physical model of lateral instability has been proposed which provides a descriptive driving mechanism of the morphology.

Acknowledgements

I would first like to extend my sincere thanks to my graduate supervisor, James A. Forrest. His wide breadth of scientific knowledge and continual guidance have been a great asset to my research. The discussions that I had with Jamie were invaluable in furthering my scientific career and expertise. Thank you for being a marvelous supervisor.

I would like to acknowledge the members of my advisory committee and my defense committee, Jean Duhamel and Jeff Chen, who provided advice and support on my research topic.

My fellow lab mates and co-workers have made my time in this degree a positive experience. I would especially like to thank the lab manager and postdoctoral researcher, Adam Raegen, for his continued guidance and aid with my project. I have learned many important skills from Adam and he has graciously passed along much of his useful knowledge to me. I am also grateful to have been mentored by Junjie Yin who has provided me with helpful discussions and a wonderful friendship. I have greatly enjoyed my time working with these people.

The technical assistance and research analysis support from Cole Lord-May has been invaluable to my thesis. Thank you for sharing your knowledge and answering many of my questions.

I would also like to thank Brenda Yasie Lee and Carina Filice for their assistance and encouragement during my graduate degree. Your help was crucial in many aspects of my life. In addition, I extend my thanks to all of the wonderful friends that I have met during my time in Waterloo for bringing joy to my life.

Finally, I am appreciative of the support system that has been present in my personal life during this experience. To my parents Warren and Wynn Trumpour, thank you for your unending love and counsel throughout this degree. To my dear friends Chanya Hughes, Sahiti Ayalasomayajula, Andrea Stout, Erin Henderson, Josie Kaip, Robert Auld, Yuriy Stankov, and Austin Mealey; I am eternally grateful for the insightful discussions and endearment that you have provided to me. I would also like to extend my thanks to my boyfriend, Andrew Gibson, for providing a sympathetic ear and irreplaceable advice during my degree. I could not imagine the completion of this thesis without all of your support.

Table of Contents

List of Tables

List of Figures

List of Variables

- N: Degree of Polymerization
- M_w: Mass Average Molecular Weight
- M_n: Number Average Molecular Weight
- $\vec{R_N}$: End-to-End Vector
- l: Bond Length
- $\langle R^2 \rangle$: Mean Squared Average End-to-End Distance
- p(N,x): Probability of End-to-End Distances
- b: Kuhn Length
- R_{max}: Maximum End-to-End Distance
- r_s: Mean Bond Vector Length
- R_g: Radius of Gyration
- $\vec{R_{CM}}$: Center of Mass Vector
- M_e: Entanglement Molecular Weight
- N_e: Entanglement Degree of Polymerization
- S: Entropy
- U: Internal Energy
- F: Free Energy or Force (specified in equations)

- T: Temperature
- k: Boltzmann Constant or Spring Constant (specified in equations)
- χ: Flory-Huggins Variable
- ϕ: Volume Density
- t: Coefficient of Transmission
- r: Coefficient of Reflection
- z: Deflection
- m: Mass
- f: Frequency
- n: Overtone
- L: Length Scale
- H: Layer Height
- ρ: Density
- R_c: Characteristic Radius
- d: Diameter

Chapter 1

Introduction

This chapter will introduce the content and background required to fully comprehend the extent of this thesis. General information about polymer physics as well as specific background related to this project will be introduced here.

1.1 Polymers

1.1.1 Polymer Basics

Polymers are macromolecule materials consisting of smaller elementary units called monomers (Figure 1.1). In fact, the roots "poly" and "mer" mean "many" and "parts", respectively[1].

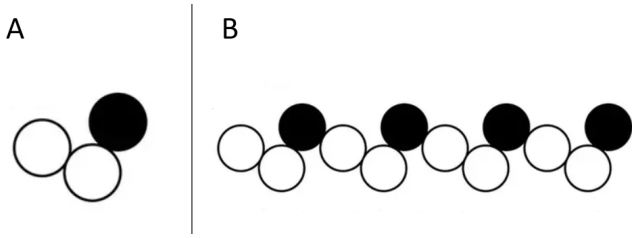

Figure 1.1: Depiction of a monomer (A) and its related polymer (B). Image taken from [2].

The monomers that make up a polymer are repeating patterns of the same base unit but may be limited to a small variety of unit types. A process called polymerization is used to convert monomers into polymers[3].

The number of repeating monomers and their distribution determines the molecular weight of the polymeric material. The molecular weight of a sample distribution can be defined in two main ways. The weight average (or mass average) molecular weight, M_w, averages the mass of the monomers over the entire sample

$$M_w = \frac{\sum N_i M_i^2}{\sum N_i M_i} \tag{1.1}$$

where M_i is the molar mass and N_i is the number of molecules of molar mass M_i within the distribution[4]. Alternatively, the number average molecular weight, M_n, averages the number of monomer chains

$$M_n = \frac{\sum N_i M_i}{\sum N_i} \tag{1.2}$$

Due to the nature of these two calculations, the mass average will always be greater than the number average molecular weight[5]. The ratio of the two molecular weights provide a value known as the polydispersity index. If M_w/M_n is exactly one, the sample is completely monodisperse, with every chain having the exact same number of repeating units. The larger the value becomes, the more polydisperse the sample[3].

1.1.2 Polymer Chain Statistics

Ideal Chains

In order to understand the nature of polymers, it is pertinent to present the theory behind their interactions. At this point the idea of ideal polymer chains will be presented and various chain statistics will be derived. This aids in a fuller understanding of the physics that drives polymer systems.

Ideal chains are chains whose conformations generate sufficient space between monomers such that there exists no interaction between them[1, 6]. Consider a flexible polymer with free joints between N monomers. Each of the backbone atoms, A_i, are connected by bonds which can be considered vectors, $\vec{r_i}$. Then, the end-to-end vector of the system is calculated as

$$\vec{R_N} = \sum_{i=1}^{N} \vec{r_i} \tag{1.3}$$

As the freely jointed model is being employed here, it can be stated that the bond length between successive atoms is constant $l = |\vec{r_i}|$. This leads into a simple statistical distribution of end-to-end distances using the mean-square average

$$\langle R^2 \rangle = \langle \vec{R_N}^2 \rangle = \langle \vec{R_N} \cdot \vec{R_N} \rangle = \sum_{i=1}^{N} \sum_{j=1}^{N} \langle \vec{r_i} \cdot \vec{r_j} \rangle \tag{1.4}$$

Applying projection formalism, the dot product can be expressed as the cosine angle between vectors $\vec{r_i}$ and $\vec{r_j}$ such that the ensemble average becomes

$$\langle R^2 \rangle = l^2 \sum_{i=1}^{N} \sum_{j=1}^{N} \langle cos\theta_{ij} \rangle \tag{1.5}$$

Specifically for the freely-jointed model, there exists no interaction between the monomers and, therefore, the average bond vectors, $\langle cos\theta_{ij} \rangle = 0$ for $i \neq j$ and $\langle cos\theta_{ij} \rangle = 1$ for $i = j$[1, 7]. Then, the mean-square end-to-end distance of an ideal chain is represented as

$$\langle R^2 \rangle = Nl^2 \tag{1.6}$$

The freely jointed ideal chain is visualized in Figure 1.2.

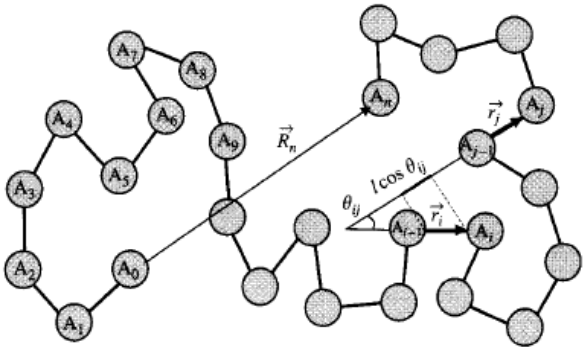

Figure 1.2: Mean-square end-to-end distance of an ideal polymer chain, visualized. Measurements and variables correspond to those in-text. Figure taken from [1].

The ideal chain model can also be easily represented as a simple random walk (Figure 1.3). Consider a basic one-dimensional lattice. The walk consists of N steps and, with each step, may progress to one of its nearest neighbors (n_+ or n_-). Each neighboring site has

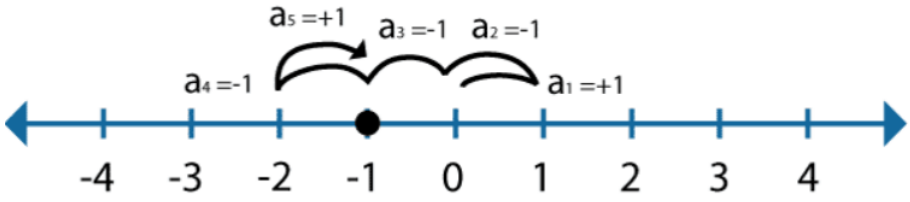

Figure 1.3: A depiction of a 1-dimensional random walk based on a number line. Each jump, a_n, represents a step taken by the walk. Figure taken from [8].

an equal probability of being walked to. Using the same variables as before, the size of the random walk is said to be $R_0 \sim N^{1/2}l$. The distribution of end-to-end vectors $\vec{r}$ then takes a Gaussian shape in one dimension, as follows[9]:

$$p(\vec{r}) = \frac{R_N}{\sum_{\vec{r}} R_N} \text{ where} R_N = R_N(\vec{r}) \text{ is the number of distinct walks}$$

$$p(N, x) = \frac{1}{2^N} \frac{N!}{(n_+!)(n_-!)}$$

By applying Stirling's approximation one obtains

$$p(N, x) = \frac{1}{\sqrt{2\pi N}} \exp\left(\frac{-x^2}{2N}\right)$$

$$p(N, x) = \frac{1}{\sqrt{2\pi\langle x^2\rangle}} \exp\left(\frac{-x^2}{2\langle x^2\rangle}\right) \tag{1.7}$$

The above result can be generalized into higher dimensions by taking the product of probabilities for each dimension. Specifically, for this project, the three-dimensional case becomes important.

Another statistic of importance for the ideal chain model is that of the effective bond length b, also called the Kuhn length. To lead into this calculation, take R_{max} to be the maximum end-to-end distance of the polymer, or the length when the chain is fully extended. Also define the mean length of a bond vector to be r_s where

$$r_s = \sqrt{\langle \vec{r_i} \rangle^2} \tag{1.8}$$

Then, with these two definitions, it is possible to put together a formula for the maximum end-to-end distance[7, 1]

$$R_{max} = N r_s \tag{1.9}$$

Using this information, along with the previous calculation of the mean-square end-to-end distance, the Kuhn length, b, is derived:

$$b = \frac{\langle R^2 \rangle}{R_{max}} \tag{1.10}$$

Apart from its importance in theoretical calculations of polymer chain statistics, the Kuhn length, in practice, corresponds to the stiffness of a polymer chain[7].

As a final statistic, the idea of a radius of gyration will be presented. The radius of gyration, R_g, characterizes the average distance between monomers and the center of mass of the polymer coil when the polymer adopts a certain configuration. This idea is in addition to that of the end-to-end distance which can be applied to any macromolecule[10]. To begin the derivation, take the radius of gyration to be the squared average length between a monomer position, $\vec{R_i}$, and the center of mass of the system, $\vec{R_{cm}}$, as

$$\langle R_g^2 \rangle = \frac{1}{N} \sum_{i=1}^{N} (\vec{R_i} - \vec{R_{cm}})^2 \tag{1.11}$$

Next, the center of mass position is defined as an average of all the position vectors within the system

$$\vec{R_{cm}} = \frac{1}{N} \sum_{j=1}^{N} \vec{R_j} \tag{1.12}$$

Combining the two formulas and inputting the double sum of squares leads to a final formula for the radius of gyration[7]:

$$\langle R_g^2 \rangle = \frac{1}{N} \sum_{i=1}^{N} \sum_{j=1}^{N} (\vec{R_i} - \vec{R_j})^2 \tag{1.13}$$

Real Chains

While ideal chains provide a general overview of the physics, polymer chains do not behave in an ideal manner within real systems. The chains no longer exhibit free rotation and simple distributions. Often, real chains are represented by a self-avoiding random walk[6]. This is still a random walk on a lattice, but the walk may never visit the same space twice [1].

The first statistical value to review for real chains is that of the total number of self-avoiding walks that consist of N steps. For large N this formula takes the form

$$\langle R_N(tot)\rangle = z^N N^{\gamma-1} \tag{1.14}$$

In this case, the values of z and γ are dependent on the dimensionality of the system. For a three-dimensional system, z=4.68. The enhancement factor, $N^{\gamma-1}$ is 1, 4/3, and 7/6 for 1, 2, and 3 dimensional systems respectively[6]. In following with this, the average root mean-square end-to-end distance can then be calculated for the real chain system to be

$$\langle R\rangle = lN^{\nu} \tag{1.15}$$

where ν is known as the Flory exponent[6]. As in previous formulas, the value ν depends on dimension and is known to be 1, 3/4, and 3/5 for 1, 2, and 3 dimensions respectively[6]. It is important to note that the size of real chains is significantly larger than those of ideal chains. The distribution function of chain lengths is no longer a Gaussian function when dealing with real chains. The behavior of the distribution becomes asymptotic at large values of R, suggesting that the chain is less likely to return to its starting point at large end-to-end distances[7]. The distribution function is shown in Figure 1.4.

Entanglement

An important characteristic of real chains is that of entanglement. This happens when the chains become long enough that they are able to interact with one another in a specific manner which creates topological constraints[11, 6]. One can imagine a mass of extension cords which have become tangled, thereby creating a constraint when you try to pull just one of them out. Entanglement effects also alter the physical properties of the polymer.

There are numerous ways to analogize and physically describe entanglement. The entangled chain can be thought of as a network strand that has been confined to a tube[1].If the tube is considered to have diameter a then the end-to-end distance of an entangled chain can be represented as

$$a \sim bN_e^{1/2} \tag{1.16}$$

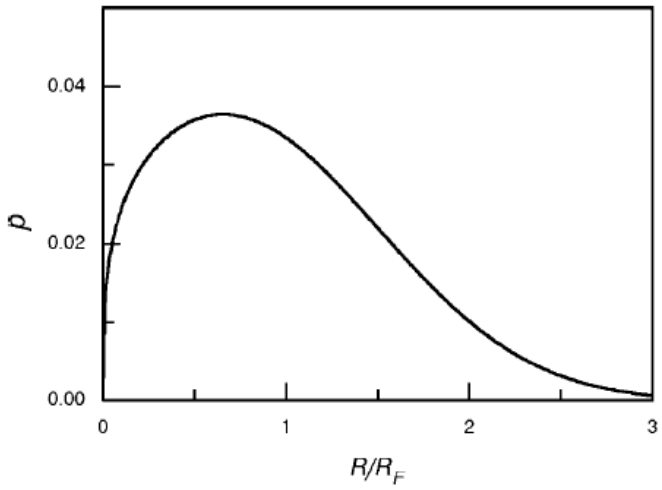

Figure 1.4: A distribution of mean-square end-to-end distances for a 1-dimensional real chain. The vertical axis represents the probability while the horizontal axis shows the particle position. R_F is the size of the polymer chain. Image taken from [7].

In another representation, entanglement is defined as a persistent contact between the mean paths of the polymer chains[12]. For either model of the entangled network, it is suggested that entangled chains dominate the topological behaviour of long polymer networks as there becomes a greater dependence on both N and the Kuhn length.

The entanglement molecular weight of a polymer, M_e is a transitional range in molecular weight whereby the polymer has qualities closer to that of a liquid below the transition and closer to that of a rubber above the transition. The rubber-like qualities are due to interaction between polymer chains such that mechanical stress may be transferred among them. For example, the stress relaxation function of a polymer tends to slow down above entanglement while the viscosity begins to increase[12]. Often, physical properties of a polymer are independent of molecular weight when they are larger than the entanglement degree of polymerization, N_e.

1.1.3 Polymer Solutions

Polymer solutions are created by mixing polymers with various solvents. Solvents are characterized by their ability to dissolve polymers and are placed into numerous categories[1]. A knowledge of solvent-polymer interactions is especially important in nanotechnology.

Processes such as wet etching and nanolithography involve the use of poor solvents to remove a masking substance or wash the surface of the substrate. Specifically, the most recent 10th generation Intel microprocessor (Ice Lake) is produced by washing the silicon chip with solvent while simultaneously attempting to maintain features smaller than 10 nm[13]. Therefore, the investigation that follows in this thesis has substantial consequences for numerous manufacturing processes. The following sections of this report will outline the experimental procedures for investigating the effects of poor solvents on polymer surfaces.

There exist various classifications of solvents when describing their ability to dissolve a solute. A 'good' solvent is characterized by its ability to completely dissolve the material's surface and bulk. A 'poor' solvent is generally accepted to have no lasting effects on the solute surface[14]. In the case of a good solvent, each molecule of polymer is surrounded by a solvent shell which effectively dissolves the polymer. However, in the case of a poor solvent there exists a preference to solvent-solvent interactions rather than that of the polymer-solvent interactions[7].

1. *Good Solvents*
   The monomer-solvent interaction is stronger than the monomer-monomer interaction.

2. *Theta Solvents*
   The monomer-solvent interaction and the monomer-monomer interaction are equally weighted.

3. *Poor Solvents*
   The monomer-monomer interaction is slightly stronger than the monomer-solvent interaction.

4. *Non-Solvents*
   The monomer-monomer interaction is stronger than the monomer-solvent interaction.

Solution Chain Statistics

Chain statistics may vary depending on the polymer solution - which model (ideal or real) of polymer chains is used, and what class of solvent it is combined with. As stated previously, the size of a random walk which represents an ideal chain in a theta solvent scales as $\sim N^{1/2}$. However, this only shows the case of an ideal system and cannot be taken as a universal relationship. The first thing to note is that polymer chains are real chains which generate some excluded volume. In this case, a polymer in a good solvent will scale as $\sim N^{3/5}$. For a real chain in a poor solvent, there exists more affinity between monomers than there does between monomers and solvent, meaning that the monomers will tend to bunch up, creating a smaller "blob" of polymer region than in a good solvent. Therefore, in this case, the size of the walk scales as $\sim N^{1/3}$[1]. Then, to summarize:

- $\langle R_\theta \rangle \approx bN^{1/2}$
- $\langle R_{good} \rangle \approx bN^{3/5}$
- $\langle R_{poor} \rangle \approx bN^{1/3}$

Flory-Huggins Solution Theory

When mixing polymers and solvents, it is crucial to have a theoretical model on which to base calculations in an attempt to understand the end result of the mixture. In 1941, Flory and Huggins simultaneously proposed a theory to explain the free energy and entropy of mixing multiple polymers together or mixing a polymer and a solvent[15, 16].This explanation is, as above, better described through a lattice model. Consider a random walk on a lattice with each lattice site occupied by one solvent molecule. Define the lattice volume density of sites occupied by monomers to be ϕ. The Helmholtz Free Energy F can then be expressed as the sum of an entropy term, S, and an energy term, U:

$$\Delta F_{mix} = \Delta U_{mix} - T\Delta S_{mix} \tag{1.17}$$

The entropy term is best understood as the number of chain arrangements that can exist for a given lattice volume density while the energy term describes the interactions between monomers and their neighbours[6]. Then, introduce the value χ which is called the Flory-Huggins variable. The variable χ represents the free energy per unit of the lattice. Good

solvents have a lower χ than poor solvents and, if $\chi = 0$, the monomer has no particular preference between other monomers and a solvent molecule[6]. For cases of large N polymers, miscibility is only possible when $\chi < 0$[17]. The final Flory-Huggins equation takes the form

$$\Delta F_{mix} = kT \left[\frac{\phi}{N} \ln\phi + (1-\phi)\ln(1-\phi) + \chi\phi(1-\phi) \right] \tag{1.18}$$

In Equation 1.18, the ϕ terms correspond to the monomers while the $1-\phi$ terms relate to the solvent. Because the entropy term is divided by N, that term has very little influence on driving mixing. While the Flory-Huggins model provides a good theoretical basic for polymer-solvent mixtures, it makes the assumption that volume does not change upon mixing, which is not true of real polymer mixtures[1].

Grafted Chains in Solvent

While the Flory-Huggins theory provides a good description of phase separation when solvents are applied to polymer systems, it doesn't examine the full picture. Grafted chain systems are often examined in the literature relating to polymer solutions. In this case the chains are directly grafted to the substrate and form various surface morphologies when solvents are introduced. Briefly, these systems are known to swell when in contact with solvents, thereby producing an energetic interaction between the swelling of the polymer and the grafted tether. This interplay of forces will often result in polymer "rich" and polymer "poor" zones which shows as a surface morphology[18, 19, 20]. Theories regarding the interactions between grafted chains and solvents will be presented more readily in the discussion.

1.2 Thin Films

1.2.1 Interactions

Polymer thin films interact in numerous ways with their surroundings. I will now focus on surface effects resultant from interactions between polymer films and solvents. A brief overview of some interactions will be presented such that the next section can expand on the surface morphologies previously investigated in the literature. In the majority of these interactions, the effect is small enough that large-scale forces such as gravity are not present.

An effect that shows up often in thin films is that of capillary roughness. When there exists a liquid meniscus between two surfaces, a capillary force is present[21]. This is the case in thin films when a solvent is placed on the surface. When the film is created through spin casting (Chapter 2) a nanoscopic roughness with a lateral length scale on the order of $\approx 2\mu m$ is induced due to the influence of the capillary force on the surface tension.

A second interaction that often results in microscale roughness is that of the Marangoni effect. Changes in the surface tension of a material caused by variations in temperature or concentration can create a morphology across the film surface[22]. When spin coating a film (Chapter 2) a surface tension gradient is formed radially outwards which may induce Marangoni instability and related roughness. The lateral length scale of this effect generally occurs on the order of tens of microns.

Over the experimental time of solvent exposure, it is often found that the films will roughen and eventually the creation of cylindrical holes will occur[23, 24]. This is attributed to an effect known as dewetting which causes holes in the film surface on a microscopic scale.

Thin films are also known to blister or bubble in the presence of different ions[25]. When an ion interacts favourably with the polymer, portions of the film may be lifted to allow ions into the surface. This will result in a nanoscopic delamination of the film surface.

The final interaction to be presented here is that of drying. As a solvent evaporates from the surface of a thin film, the shear stress of the system will cause the surface to crack[26]. The cracks appear to be nanoscopic in scale but appear across the entire surface.

1.2.2 Morphologies

Although the effect of solvents on the roughness of polymer thin films has been previously investigated, it has rarely been characterized on a nanoscopic scale. Before introducing the project at hand, one must understand the previous work that has been completed in this field.

Previously, studies have examined the various morphologies present within polymer thin films. Karim *et al.* investigated the phase-separation surface morphology present in polymer blends due to temperature[27]. The film covering the surface had a topology that revealed a pattern amplitude of 250 nm and lateral size of 2μm in diameter. The morphology found by Karim *et al.* was attributed to a critical temperature lateral phase separation of the polymers present in the blend, beginning with droplets and slowly morphing into a lateral pattern. Xue *et al.* performed similar experiments, instead inducing a

spinodal instability in the films through a perturbing field[28]. Here, the resultant structure was even larger with a lateral length scale of 8μm. Strawhecker and Kumar performed a study in which it was found that the Marangoni effect of solvent evaporation from thin films could be avoided by adjusting the evaporation rate[29]. Here, the authors found that Marangoni-induced surface roughening occurred on the scale of 10μm. More recently, Fowler *et al.* investigated surface morphology present due to the drying of spin coated films which showed the Marangoni effect[30]. It was found that temperature induced the Marangoni instability and led to a morphology with amplitude of 50 nm and length scale of 30 μm. While all of these results showed interesting forms of phase separation and the production of surface morphologies, the majority of this literature presents results on the microscale that, in the present day, are fully understood.

Previous work that has examined the interactions between polymer thin films and solvents on the nanoscale are less prevalent in the literature. de Gennes formulated a theory which describes when a thin film becomes rough after evaporation of a high vapour pressure solvent[26]. Furthermore, he determined that, during evaporation, polymers create a polymer-rich crust on the surface from the solvent-induced swelling and then prompt collapse of the polymer chains. Perlich *et al.* found that a small amount of solvent consistently remains in the film after evaporation during spin casting[20]. This implies that the remaining solvent swells the polymer surface and creates a surface morphology. Moreover, it was determined through neutron reflectometry that the leftover solvent amount increases with increasing molecular weight and thickness of the polymer film[20]. In 2001, it was shown that solvents produce ridges in the film rather than a crust or blistering effects and it was seen that the intensity of the morphology was dependent on the volatility of the solvent[31]. No particular interaction was attributed to this morphology. A recent study by Statt *et al.* performed a molecular dynamics simulation which investigated poor solvents on polymer thin films[14]. This paper was published based on previous work completed by my group. Both monodisperse and polydisperse systems were considered along with a range of solvent qualities. It was then supported that both the roughness and interfacial width increased with increasing solvent quality (Fig 1.5). While the Statt paper provided the relation of surface morphology to solvent quality, it shows few results in the way of length scales, amplitudes, or other characteristics of the morphology. Further, the work only dealt with small N chains and it is not clear how to fully compare that to the work of this thesis.

Theories based around polymer brushes and their interactions with poor solvents are more prevalent in the literature than that of thin film studies. Polymer brushes are chains which have been grafted by one end onto a substrate, similar to the grafted chains which were previously introduced. Theoretical treatments of these types of systems revolve

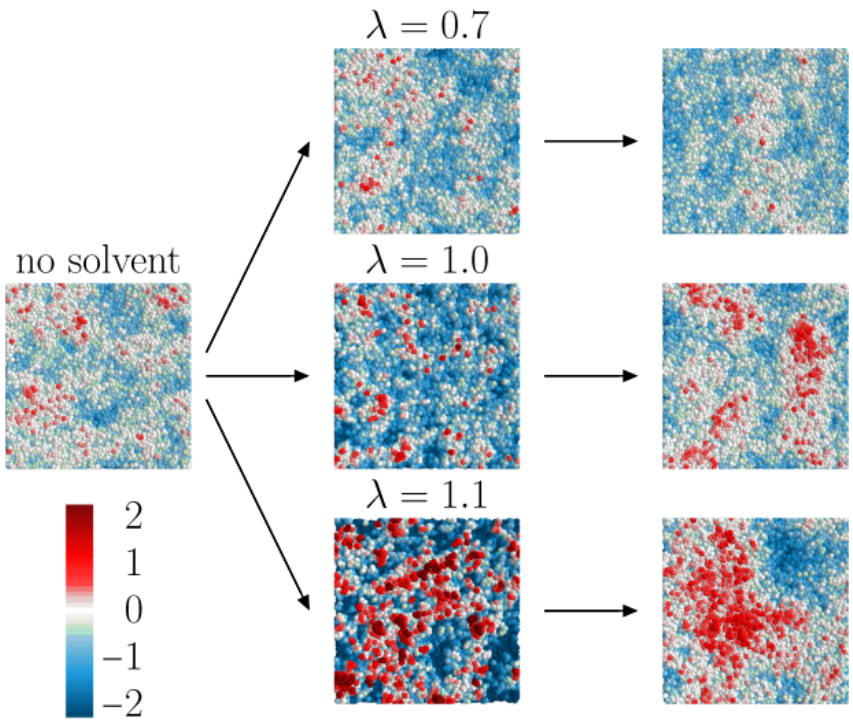

Figure 1.5: An image of results from the Statt *et al.* work relating solvent quality, λ to the surface roughness. The colour indicates the relative height of the monomers in the simulation and the arrows indicate the progression of time through the simulation (solvent present, evaporation, and crust formation). Image taken from[14].

around the optimization of free energy and entropy effects which lead to lateral instabilities in the film surface. Further examination of these theories will be completed in the discussion.

Based on the literature review of solvent-polymer interactions, it is clear that there exists no unifying theory to explain surface roughness resultant from solvent effects. Further, there is little information regarding the formation of nanoscopic morphologies due to the presence of poor solvents. These points then motivate the goals of this thesis. To the best of my knowledge, this thesis presents the first experimental study which investigates nanoscopic surface roughness due to the exposure of polymer thin films to poor solvents.

Chapter 2

Techniques

This chapter will provide an overview of the methods and techniques applied to this thesis. I will present the materials used in the sample preparation as well as the characterization methods utilized to provide results.

2.1 Sample Preparation

The process for creating polymer thin films is well known in the polymer science field and was followed closely for this experiment. As a general overview, the polymer is first dissolved in a good solvent to make a low percentage solution of polymer-to-solvent by mass. The solution is then deposited by pipette onto a substrate and spin-coated to create a film of uniform thickness. The exact amounts and process of creation for this project are detailed in the following sections.

2.1.1 Polymers

Polystyrene (PS) is a commonly used material due to its widespread abundance and thoroughly investigated properties[7, 32]. The physical properties of PS make it a desirable substance to use in morphology experiments as it tends to have a low amount of crystallinity and is often brittle due to its stiff carbon backbone. PS is a polymer consisting of a carbon backbone and phenyl side groups (Figure 2.1). Reported molecular weights between entanglements (M_e) for polystyrene range between 23 000 g/mol and 30 000 g/mol[11].

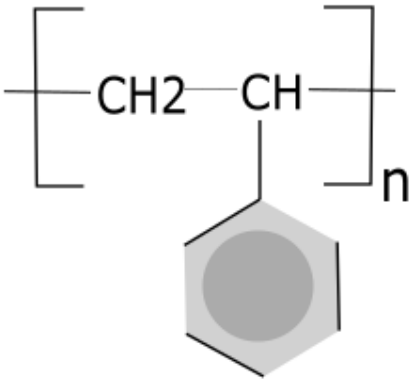

Figure 2.1: A schematic of one monomer of polystyrene, where n is the number of repeats.

Another commonly used polymer is Poly(Methyl Methacrylate) (PMMA). The M_e values for PMMA runs from 9200 g/mol to 13 750 g/mol[33]. A schematic of PMMA is shown in Figure 2.2.

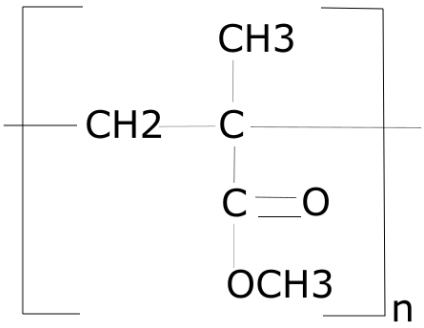

Figure 2.2: A schematic of one monomer of PMMA, where n is the number of repeats.

Nine number average molecular weights of polystyrene were chosen for this experiment. Solutions of each molecular weight sample were prepared as a 2% PS-to-Toluene solution in preparation for a spin coating procedure. M_n values were: 995 kg/mol, 545 kg/mol, 83 kg/mol, 44.6 kg/mol, 21 kg/mol, 16.4 kg/mol, 11.5 kg/mol, 10.5 kg/mol, and 8 kg/mol. The molecular weights were selected to examine solvent-induced morphologies for M_n values of polystyrene that were smaller and larger than M_e. All of the samples were purchased from Polymer Source Inc. and had polydispersity indices ranging from 1.05 to 1.2. Once

the solutions had been prepared they remained undisturbed for 24 hours to ensure that the solution was fully mixed at the time of spin coating. The resultant solutions were clear, transparent liquids.

Solutions of 2% PMMA to Toluene were prepared in the same manner as the PS solutions. Two number average molecular weights of PMMA were used as a proof of concept: 405 kg/mol and 10 kg/mol.

2.1.2 Spin Coating

Spin coating is a simple and versatile method for preparing thin films. First, a polymer is dissolved in a good solvent and is then deposited onto a substrate surface which is spun at high speed[34]. The thin films created by this process are often uniform in thickness. For a constant molecular weight and solution concentration, the thickness of the film is dependent on the rotation speed and will visually appear as a variation in colour (Figure 2.3). The colour difference is due to wavelength interference created by the Fresnel effect. When light passes through a smooth boundary between materials of two different refractive indices, the alternative reflection and transmission will lead to a color variation (Figure 2.4)[35, 36].

Figure 2.3: A depiction of the visual colour difference in polymer thin films of ranging thickness. The thickness increases from right to left.

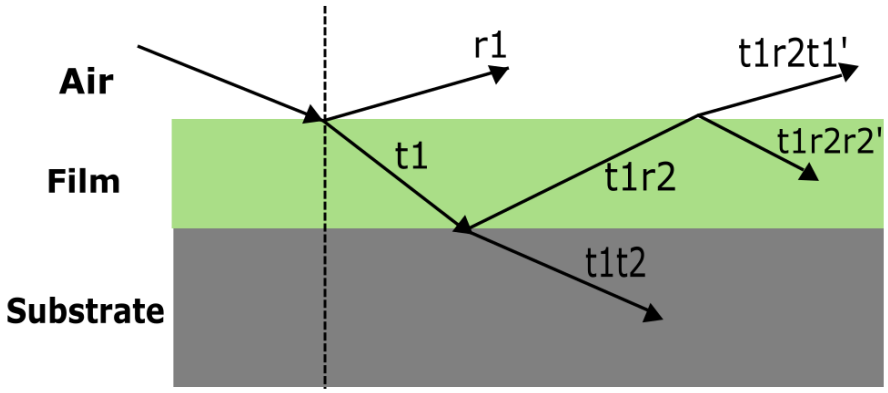

Figure 2.4: A graphic of the Fresnel effect in a thin film. The incident beam will split into various transmissions and reflections, $t(n)$ and $r(n)$, which interfere when they reach the viewer's eye. The coefficients depend on the thickness and related refractive index of the thin film.

For this project, solutions were deposited on 1 cm^2 wafers of $\langle 100 \rangle$ silicon in a speed range of 900 rpm to 2500 rpm. The final polymer thin films ranged in thickness from 100 nm to 130 nm.

2.1.3 Solvent Exposure

All molecular weights of PS and PMMA were exposed to poor solvents for the purpose of creating nanoscopic surface morphology. The experiments for PS were in-depth and tested a wide range of molecular weights while those for PMMA were simply a proof of concept and were less rigorous. Each molecular weight sample was exposed to numerous poor solvents over a range of exposure times to test for multiple variables. A simplified table of the experimental solvent exposure procedure is shown in Table 2.1.

The varying exposure times were completed with two different methods. The 'drop while spinning' exposure consisted of dropping the solvent onto the thin film while the stage was already at speed. The '5 second exposure' method consisted of dropping the solvent onto the thin film, waiting for 5 seconds, then spinning the system at the required speed.

Polymer	Poor Solvent	Exposure Time
Polystyrene	Pentane	Drop While Spinning
Polystyrene	Pentane	5 Second Exposure
Polystyrene	Heptane	Drop While Spinning
Polystyrene	Heptane	5 Second Exposure
Polystyrene	Dodecane	Drop While Spinning
Polystyrene	Dodecane	5 Second Exposure
PMMA	Methanol	5 Second Exposure
PMMA	Propanol	5 Second Exposure

Table 2.1: A table describing the experimental setup for solvent exposure. Each solvent-exposure time combination was completed for all molecular weights of both PS and PMMA.

2.2 Atomic Force Microscopy

The main principle for the operation of an AFM is the measurement of force as a needle placed at the end of a cantilever is translated across the sample surface (Figure 2.5).

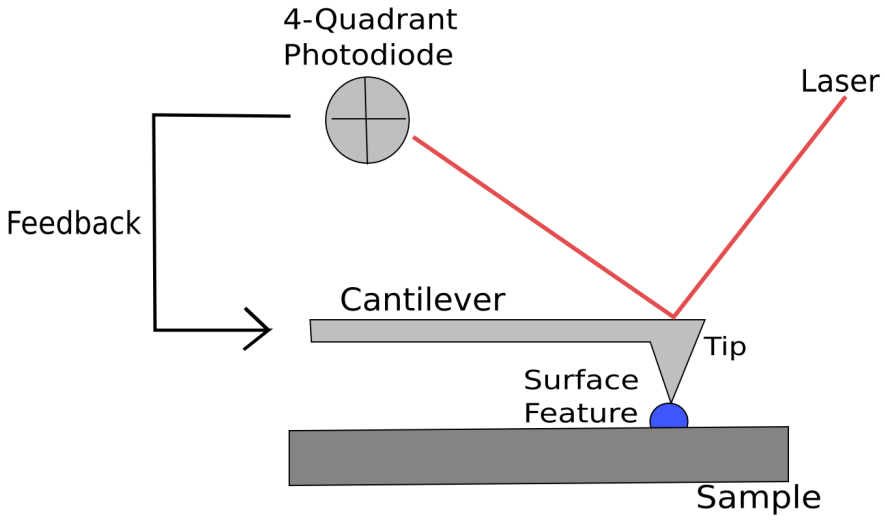

Figure 2.5: A schematic depiction of a typical AFM setup.

When the cantilever is deflected over the surface roughness, a photo diode is used to sense the movement and send this signal to a computer[37]. Hooke's Law is applied with

knowledge of the lever stiffness to calculate the force of the interaction

$$F = -kz \tag{2.1}$$

where k is the cantilever stiffness, z is the measured deflection, and $-F$ is the calculated restoring force[38, 39].

In an AFM system, the measurement of the tip deflection is completed through laser reflection. A laser beam is focused onto the top of the cantilever tip and is reflected back onto a detector. This detector is usually a photo diode[37]. The diode is divided into four quadrants and the laser is initially centered to define zero tip deflection. As the tip is bent or deflected by the surface, the laser will be moved into different areas of the photo detector. Computer software then uses the difference in laser position on the detector to engage a proportional-integral-derivative (PID) feedback loop[37, 40]. The deflection of the tip will be minimized by the PID such that a restoring force is applied to the tip, thereby ensuring that the deflection is nearly always at zero. This feedback loop ensures that the tip moves along the surface at a given parameter such as constant force or constant height[40].

An AFM is mostly operated in one of three main modes. These are commonly referred to as contact mode, non-contact mode, and tapping mode. In contact mode, the cantilever is pulled across the sample surface while the feedback loop maintains a constant deflection with respect to the sample, allowing for the measurement of force using Hooke's law. The output of this mode results in a topographical map of the surface[39, 40]. For non-contact mode, the cantilever tip is purposely kept at a fixed distance away from the sample while being oscillated close to its resonance frequency. This mode can measure the shifts in vibration from the natural frequency and is able to provide information on the amplitude, phase, and frequency of the tip oscillations. The variation from the resonance frequency is related to the force and the computer will provide a topographical output[39, 40]. The advantage of using an AFM in non-contact mode is that it provides less invasive imaging such that the tip does not usually ruin the sample being imaged. The third mode that is commonly used to operate an AFM is tapping mode. This operation combines the effects of contact and non-contact allowing for the tip to be oscillated at resonance frequency while also maintaining contact with the sample surface. This method allows for topographical outputs of samples that may have friction or adhesion, causing problems in other modes[40]. Through the previously discussed feedback loop and a piezo actuator, the amplitude of the cantilever tip oscillation is held constant in tapping mode[40]. Similar to the non-contact mode, tapping mode can produce images of amplitude, phase difference between the cantilever and the driving piezo, and the topography[41, 42]. A typical topography created from tapping mode AFM is shown in Figure 2.6.

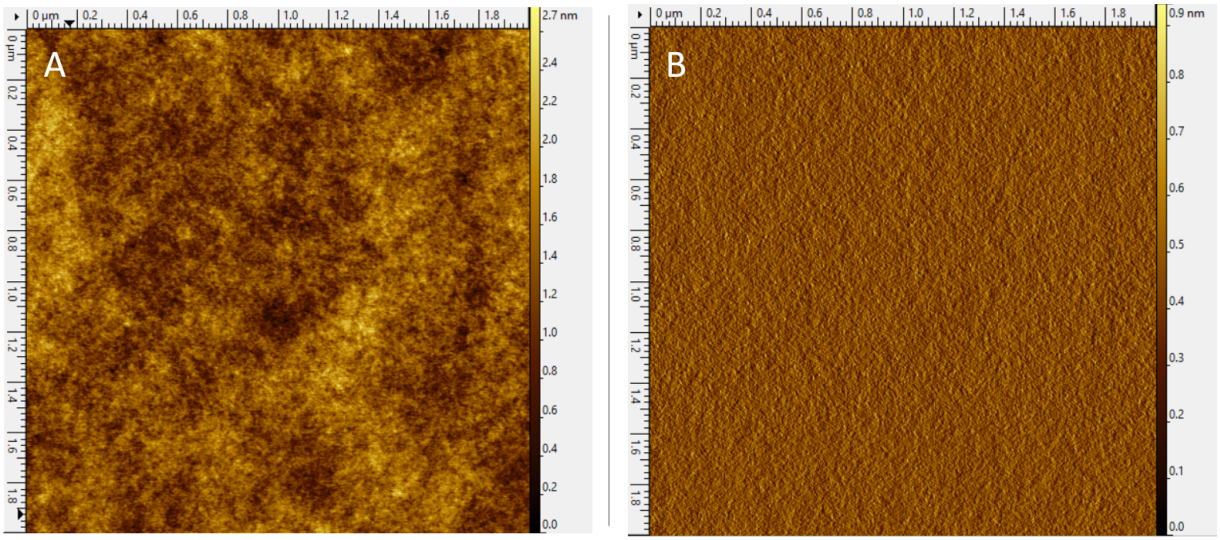

Figure 2.6: A 2 μm size AFM image of the topography of a thin polymer film. Image (A) depicts the height scan while image (B) shows the phase. The phase image represents a change in the frequency of the tip such that the resonance frequency is not in phase with the frequency of running across the sample. This type of image generally visualizes effects due to forces such as adhesion or stiffness of the sample.

In the project presented here, after the entire range of samples had been exposed to solvent, AFM was used to garner topographic information regarding the surface morphology of the films. The JPK Nanowizard 3 BioAFM was used in tapping mode to image the samples over 3 scan sizes. Each sample was imaged at 10 μm^2, 2 μm^2, and 1 μm^2 such that the surface could be examined at a variety of length scales. The scan rate was then altered for each successive scan size such that the tip was moving over the surface at the same speed.

2.3 Quartz Crystal Microbalance

A QCM-D is a tool which measures mass and structural change in a sample through the use of a vibrating quartz crystal that is placed between electrodes (Figure 2.7).

The oscillation resonance frequency changes depending on the mass change per unit area of the substrate. In this manner, adsorption or swelling effects are able to be studied with this tool[43]. QCM-D works on the principle of the piezoelectric effect, in which an

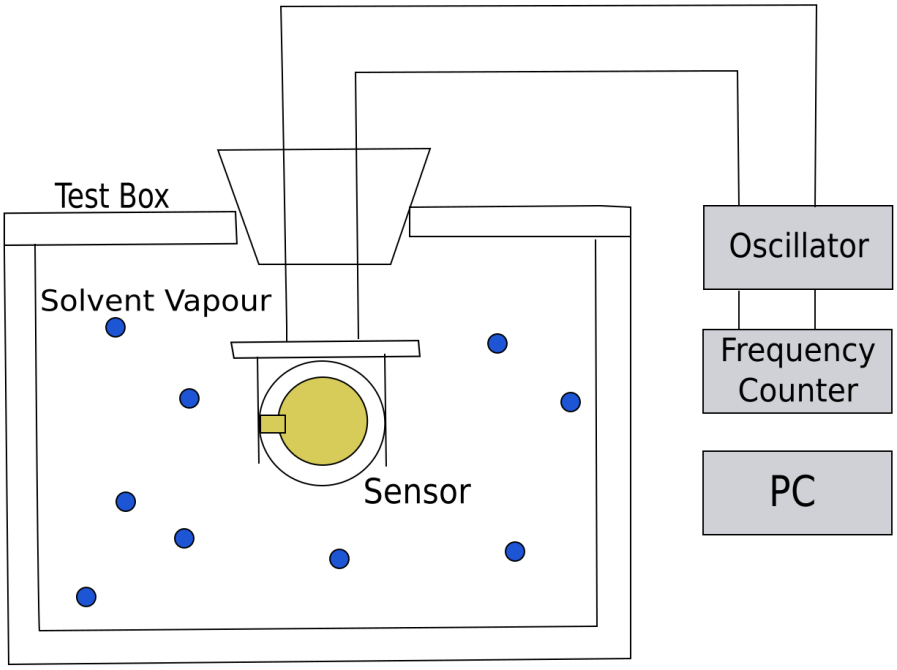

Figure 2.7: Schematic depiction of a typical QCM setup.

electric signal is converted to mechanical motion. Since the quartz crystal has a resonance frequency any effects that produce a physical motion off-resonance will appear as a peak in the frequency sweep data. Generally, the mass change on the crystal can be calculated using the Sauerbrey equation which relates a change in frequency to a mass change per unit area[44]. The equation is

$$\Delta m = \frac{-C\Delta f}{n} \tag{2.2}$$

where m is mass per unit area, C is a constant that depends on crystal properties, n is the overtone, and f is the frequency. For the type of crystal used in this thesis (5 MHz at room temperature), the constant is $C = 17.7$ ng/cm^2[45].

As a measurement of surface swelling for this thesis, a Q-Sense QCM-D was used to examine the mass change in the thin films when exposed to a poor solvent. The previously described polymer-toluene solutions were spin cast onto gold coated QCM-D crystals to create a thin film. The crystal was then connected to an open-air system. A background

reading for the thin film without solvent was taken to ensure a baseline measurement. To expose the film to a poor solvent vapour, a Kim Wipe^{TM} was dampened with the desired solvent and placed into the bottom of a 250 mL beaker. The beaker was inverted over the open-air portion of the ACM system, and Parafilm^{TM} was wrapped around the base to ensure a good seal. Thus, the QCM-D crystal and, therefore, the polymer thin film was exposed to poor solvent vapour. The system was left to measure the mass change until the system was at equilibrium. At this point, the beaker was removed and the system was allowed to recover. This process happened over a long time period ranging from 1 hour to 20 hours, depending on the solvent. The Sauerbrey equation was chosen for analysis of the QCM results as it provides a good approximation to the case of QCM in solvent vapour, rather than in pure liquid.

Chapter 3

Experimental Results

What follows in this chapter is the data resultant from experiments completed throughout this thesis. I will present the raw data, methods utilized to analyze the results, and final interpretations.

3.1 AFM Results

Visuals of the AFM results presented in coming sections are shown in Figures 3.1 through 3.4.

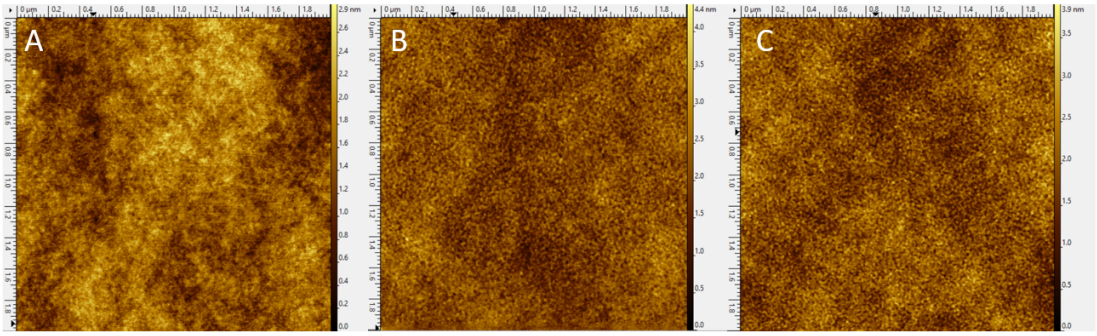

Figure 3.1: AFM images of PS to compare different exposure times. The M_w of 545 000 g/mol and the solvent, heptane, remain the same across all images. Image (A) shows the background, or no solvent, case. Images (B) and (C), show surface morphology induced by a 5 second exposure and a drop while spinning, respectively.

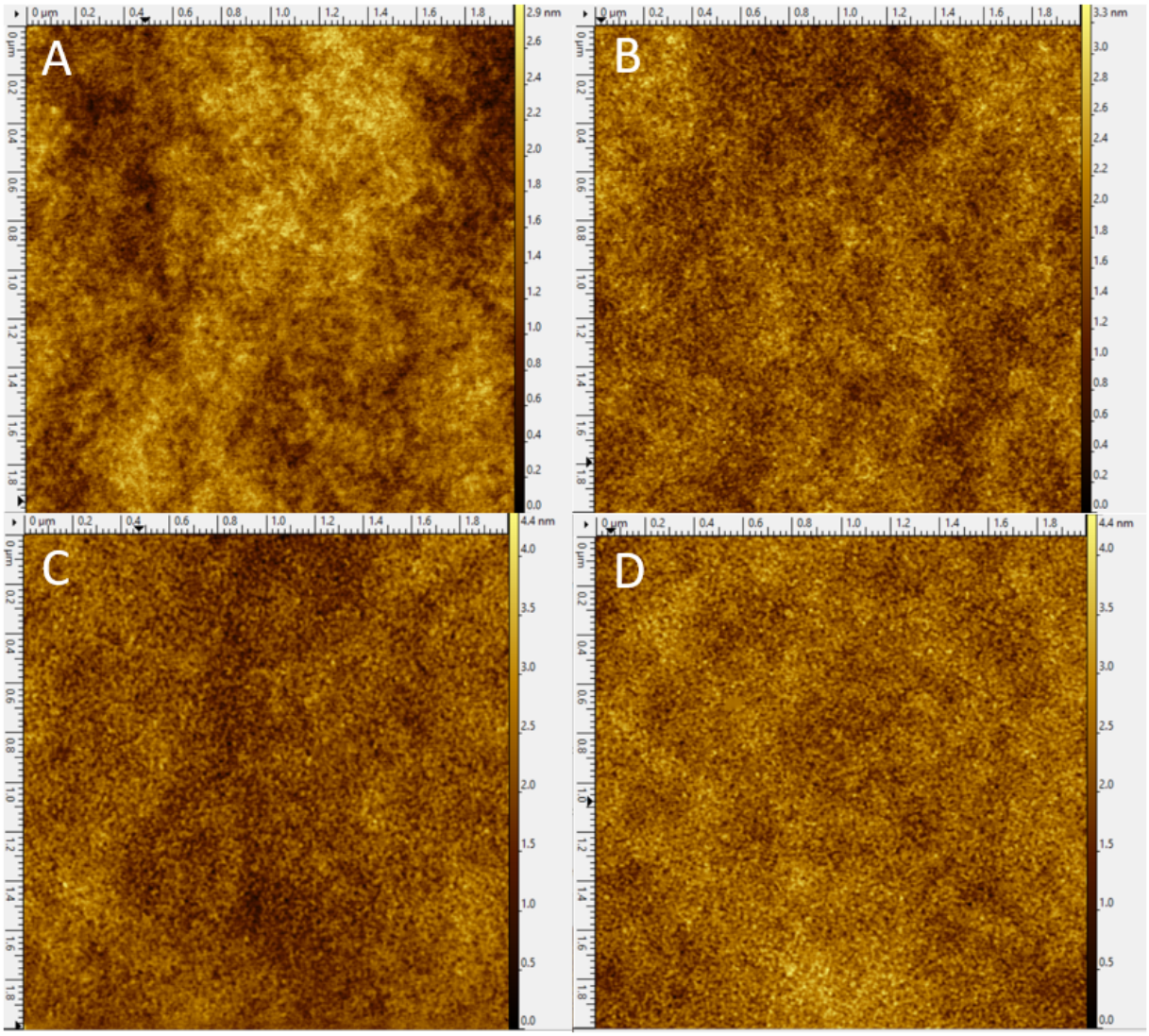

Figure 3.2: AFM images of PS to compare different poor solvents. The M_w of 545 000 g/mol and the 5 second exposure time remains constant across all images. Image (A) shows the background, or no solvent, case. Images (B), (C), and (D) show surface morphology induced by dodecane, pentane, and heptane respectively.

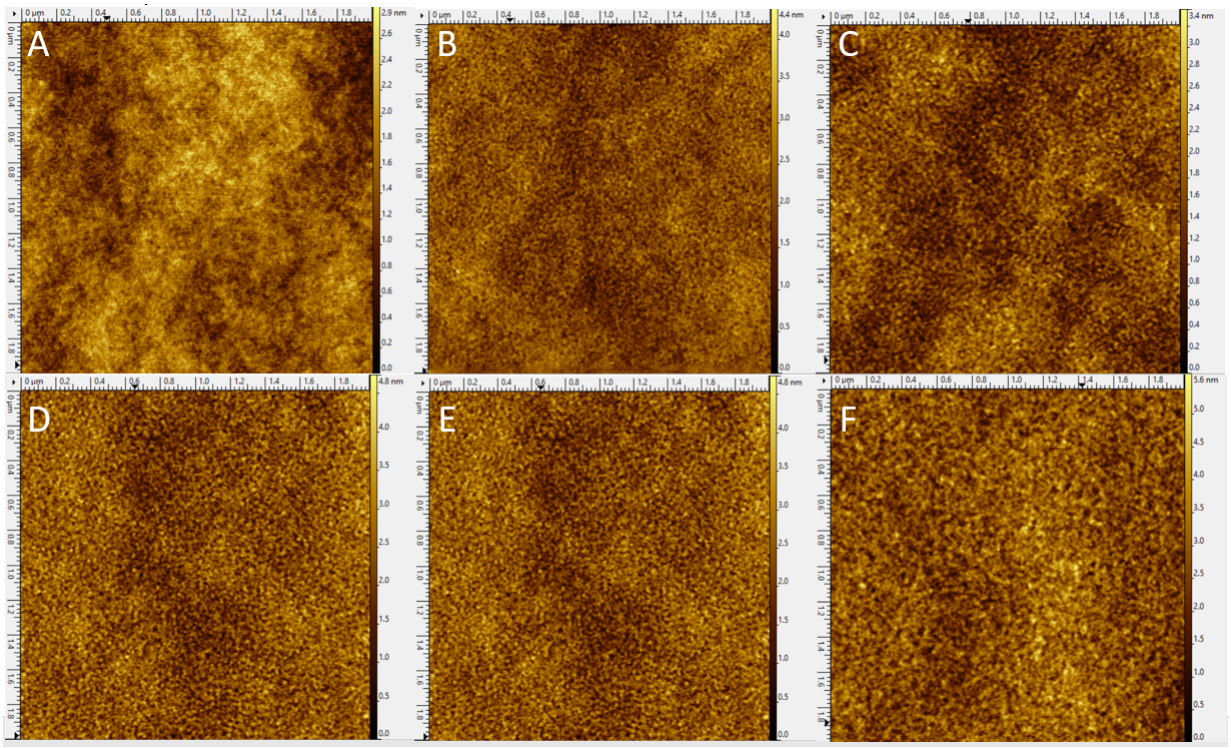

Figure 3.3: AFM images of PS to compare different molecular weights. The exposure time of 5 seconds and the solvent, heptane, remain the same across all images. Image (A) shows the no solvent case. Images (B), (C), (D), (E), and (F) show surface morphology induced for 545 000 g/mol, 83 000 g/mol, 44 000 g/mol, 21 000 g/mol, and 16 000 g/mol respectively.

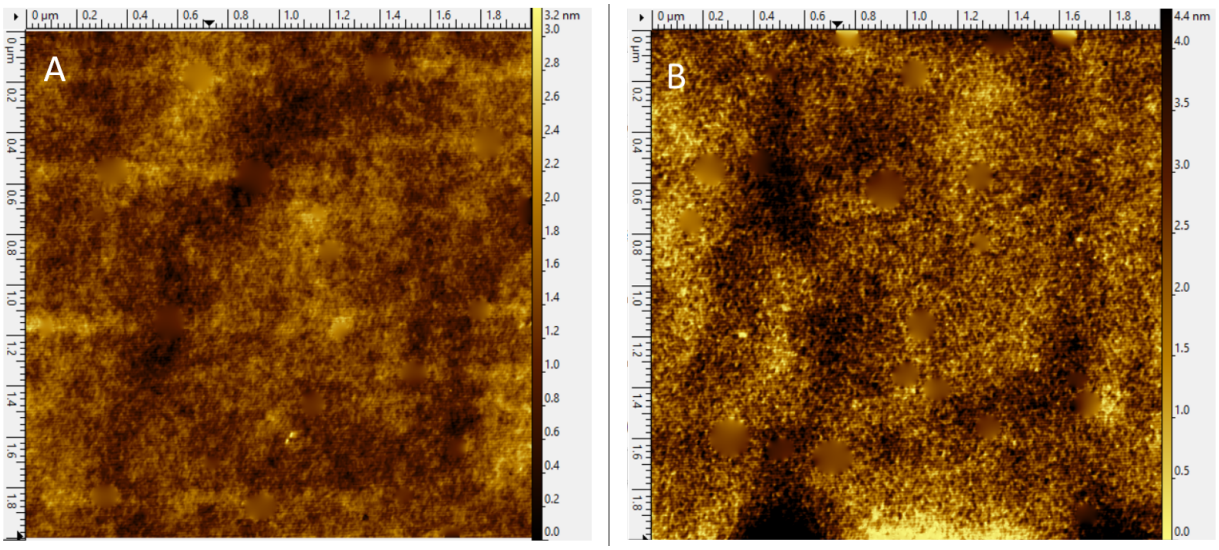

Figure 3.4: AFM images of PMMA with a M_w of 405 000 g/mol. Note that both samples had dewet over time and the blurry, circular regions on the images were fixed in post-processing to ensure a proper visual of the thin film surface. The background image is shown in (A) while (B) was treated with methanol for 5 seconds.

3.2 Image Analysis

This section provides an overview of the methods used to obtain quantitative results from the AFM images. The first part of the processing used an image analysis software called Gwyddion to convert the .jpk files output from the AFM to .txt files that could be read by a custom script. The files were then passed through a custom code to determine a characteristic length scale present in the topology of the polymer films.

3.2.1 Gwyddion Processing Trials for Length Scale

The first step for all image analysis was to level the AFM images along each line scan with a first degree polynomial. This was completed such that the topology could be calibrated against a reference sample, allowing for accurate visualization. Visually large scars or defects were removed from the image by interpolation of the surrounding regions. In an attempt to quantify the characteristic length scale that was visually present in the AFM morphology, numerous statistical analysis methods were attempted. This was a non-trivial process and the three attempts at extracting length scales are described in the following paragraphs.

A first trial consisted of using a "roughness" parameter to extract the mean squared deviation in height from a one-dimensional evaluation line

$$R_{rms} = \sqrt{\frac{1}{N}\sum_{i=1}^{N} r_i^2} \tag{3.1}$$

where N is the number of points sampled along the line and r_i is the height deviation from the mean of the line. This method failed to fully examine the desired morphology as it averaged the roughness over a large area (many lines) and would only output height deviations. This method was then discarded as a way to determine the characteristic length scale of the topology.

Another attempt at length scale extraction involved the fast Fourier transform (FFT) of the image and combining it with a radial analysis. On the most basic level, the FFT transforms all points on the image from the spatial domain to the frequency domain. The Fourier transform is a mathematical process that represents a function, $f(x)$, as a combination of sines and cosines, as follows:

$$F(u,v) = \int_{-\infty}^{+\infty}\int_{-\infty}^{+\infty} f(x,y)e^{-2\pi i(ux+vy)}dxdy \tag{3.2}$$

Due to the radial symmetry of the FFT, it was determined that the best way to compare the background images with those that were solvent treated was to take a radial average over the theta direction (in spherical coordinates) of the FFT images (seen in Figure 3.5). While the resultant plot showed a bump, there was not a distinct difference between the treated and untreated samples, rendering this method a failure.

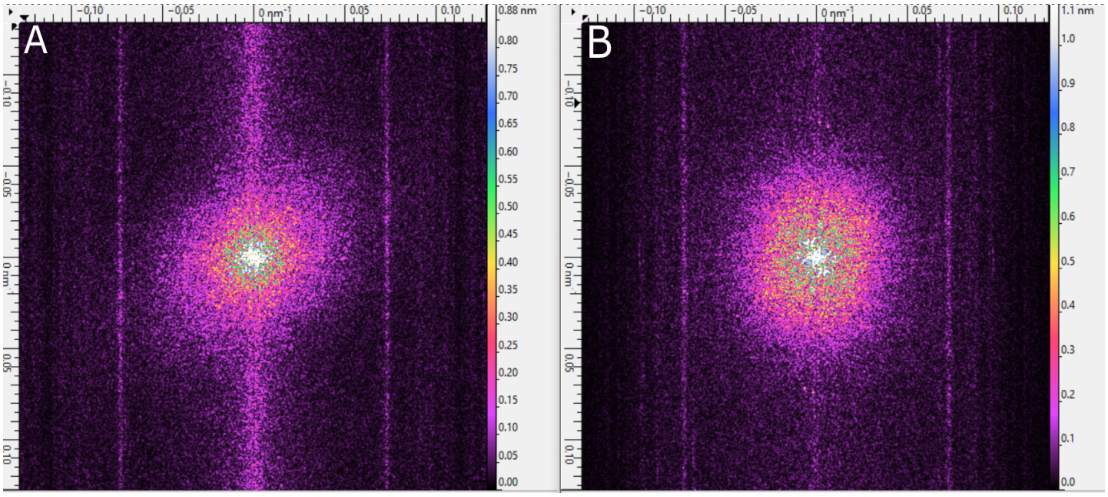

Figure 3.5: FFT outputs of an untreated sample (A) and a solvent-treated sample (B).

The final, successful attempt at analyzing the length scale of AFM images utilized the radial power spectral density function (PSDF). A short mathematical description of the radial PSDF is that it is an FFT of the auto-correlation function of the image, radially averaged over the peaks such that any spherical aberration is nullified. The formula for the PSDF which was applied to the samples used for this thesis is

$$\omega(k_x, k_y) = \frac{1}{4\pi} \int_{-\infty}^{+\infty} \int_{-\infty}^{+\infty} G(\tau_x, \tau_y) e^{-i(k_x \tau_x + k_y \tau_y)} d\tau_x d\tau_y \tag{3.3}$$

where $G(\tau_x \tau_y)$ is the two-dimensional auto-correlation function of the image. Briefly, this means that the PSDF shows which points in frequency space exhibit the least amount of variance over delay times, τ[46]. Since, in Fourier space, each point shows a specific frequency from the original image, the PSDF shows peaks of differences in frequencies (characteristic differences)[47]. An alternative way of thinking about this is that the periodic structure present in the spatial domain of an image is represented by peaks in the PSDF[46]. Therefore, using Gwyddion to complete the two-dimensional radial PSDF of

each image allowed for successful determination of characteristic length scale. It is postulated that the PSDF showed results more distinctly than the FFT because the FFT is directionally oriented in the x and y planes whereas the autocorrelation, which the PSDF is based upon, is direction-independent. Further, due to similar reasoning, the PSDF is mostly unbiased by the scan size and pixel resolution chosen by the end user[48]. An output of the radial PSDF on a treated sample is shown in Figure 3.6.

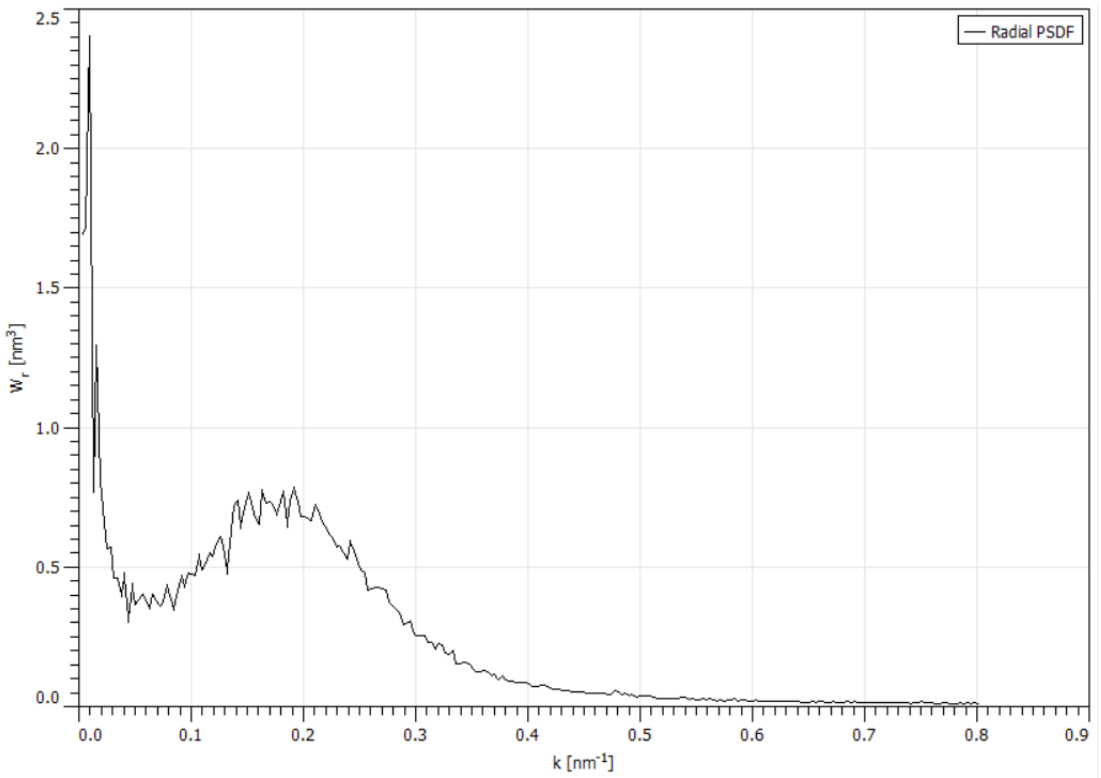

Figure 3.6: Radial PSDF of a solvent treated sample with nanoscopic morphology. The x axis shows inverse size while the y axis shows the "power" at each value. The distinct bump at 0.2 nm^{-1} is indicative of a characteristic length scale.

3.2.2 Code Analysis for Length Scale

After the radial PSDF was computed in the Gwyddion software, a text file of the output plot was exported to be used in a custom analysis code. Reasoning for this stems from the

fact that Gwyddion is unable to compare plots between samples. A script was written in the Python language to import the .txt files of the radial PSDF plots. The background (no solvent added) data was then fit to a function. The fitting function was determined to be

$$y = ax^{-2(1+h)} + c \tag{3.4}$$

where y is the resultant data, x is the input data, and a,h, and c are variable to the fit. The form of the fitting function was determined through some trial and error while adapting fit results from much of Ophelia Tsui's work[49, 50, 51, 52, 53]. Once the background (no solvent treatment) was fit, plots with the addition of solvent were passed through a Savitzky-Golay filter to smooth the data. The two plots were then compared and a length scale was determined. The characteristic length scale of the images corresponds to the point where the peak of the treated data sits on the x-axis (Figure 3.7).

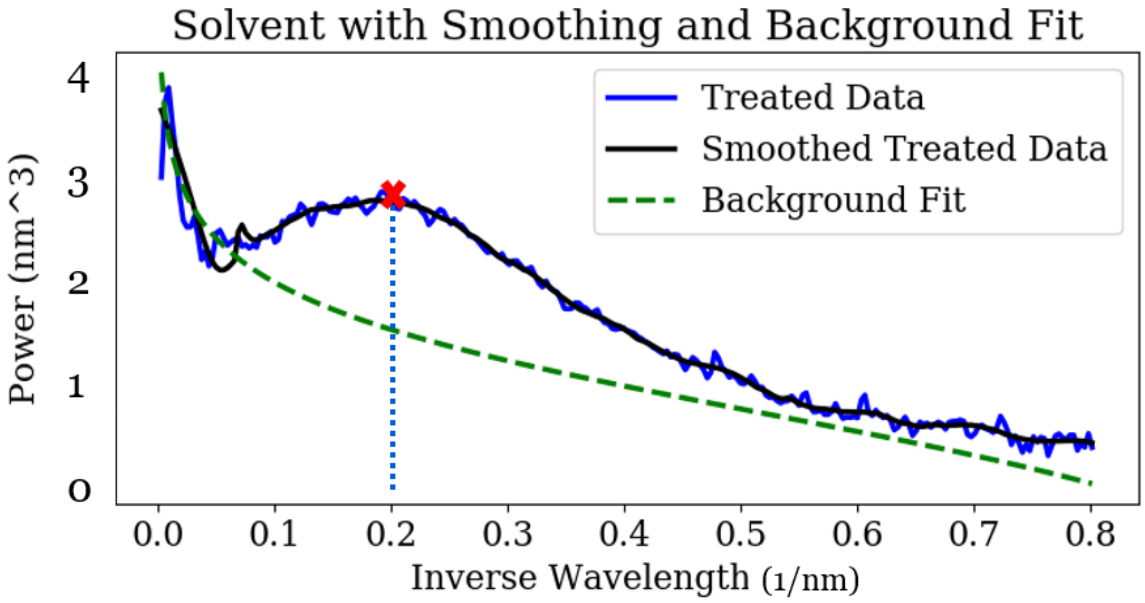

Figure 3.7: A figure output from the custom script which illustrates the background PSDF which shows the polymer-toluene solution (green dashed line) compared to the smoothed, poor solvent treated data (solid black line). A red 'x' indicates the peak of the bump in the PSDF used for length scale calculation.

This is made simpler for the script by subtracting the background such that the peak can be defined. However, due to the FFT nature of the radial PSDF, there exists a factor

of 2π that must be added to the calculation. If we set the desired point along the x-axis to be 'x', then the length scale, L, is determined by

$$L = \frac{2\pi}{x} \tag{3.5}$$

Due to the automation of the calculations from the Python script, length scales for all samples could be computed efficiently. The full custom script is available in the Appendix.

3.2.3 Gwyddion Processing for Amplitude

To extract the bump amplitudes from the AFM images, 5 different line profiles were taken across the surface of the images. Each profile was less than 1 μm in length such that the capillary roughness was not included. On each of the 5 lines, 3 different amplitude maxima were extracted. To clarify, 3 maximum peak to peak distances were taken from the line profile. A depiction of one such line profile is shown in Figure 3.8. The peak to peak amplitudes were averaged over the 3 points to create an average peak to peak distance for each of the 5 line profiles. From here, an overall average of peak to peak amplitude was calculated over the 5 line profiles. This process was completed for each sample, including both the background and solvent treated films. From the final results for each solvent treated sample, the background average was subtracted to isolate the nanoscopic bump amplitude.

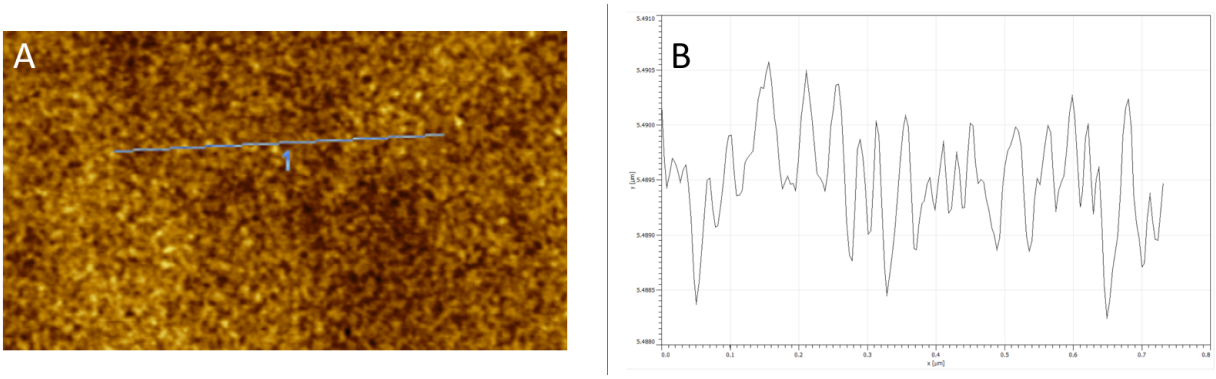

Figure 3.8: A line profile taken across a solvent treated sample. Image (A) shows the line utilized while (B) shows the output. The axes in (B) correspond to the horizontal and vertical spacial features of the surface. Both axes are in units of μm.

3.3 Overall Results

Once all of the AFM images had been processed, the data was compiled into overall results. The two main outputs from this project are the characteristic length scale of the nanoscopic morphology (x-y axes of the AFM image) and the bump amplitudes (z axis of the AFM image). Moreover, to generalize the results by including a further set of polymers, the results were completed for both PS and PMMA. In the final section of this chapter, brief results from the QCM-D swelling experiment are presented. These provide further information and reasoning regarding the results of the solvent-induced morphology.

3.3.1 Characteristic Length Scale

The combined results for the characteristic length scale of the solvent-induced morphology are shown in Figure 3.9.

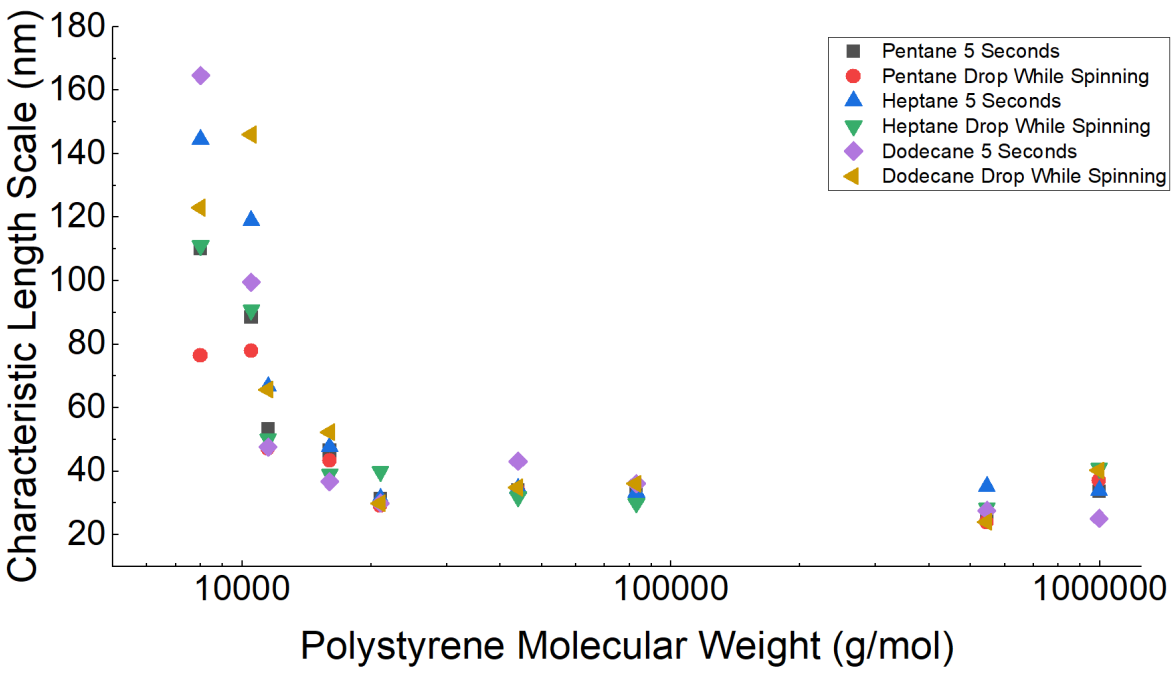

Figure 3.9: Plot of characteristic length scale as a function of molecular weight, solvent, and solvent exposure time. The x-axis follows a logarithmic scale. Error bars were calculated but left off the plot for visual sake.

From Figure 3.9 a number of conclusions may be drawn. The first thing to notice is that there exists a change in trend near 20 000 g/mol molecular weight. Prior to this point there is a distinct, approximately exponential decay while afterwards there seems to be an approximately linear trend. For this study, this result may be attributed to one of two things. The first is that the critical behaviour revolving around the entanglement molecular weight of $\approx$ 30 000 g/mol for PS changes the trend of the plot. The morphological length scale is molecular weight-dependent prior to entanglement but independent afterwards. This result is easily explained by entanglement as the polymer chains are more susceptible to solvent molecules surrounding them while they are not entangled with one another. Indeed, it was confirmed by Yeung *et al.* that the distance between entanglement points is much larger at low M_w[54]. A secondary explanation is that of polymer solubility. Recall the Flory-Huggins formula of mixing with the Flory parameter χ describing the mixing interaction and, therefore, relating to the solubility. Because χ does not show a strong M_w dependence, the entropic term of the Flory-Huggins relation dominates the solubility of a polymer[55]. Expanding this idea, it is understood that lower M_w polymers have more entropic contribution of rearrangements and will, therefore, be more soluble. This indicates that, while the "poor" solvents may be poor for large M_w, they have a significant dissolution effect at low M_w.

The next realization that results from the plot is that the 'drop while spinning' samples have a tendency, when compared with the 5 second exposure samples, to create a larger characteristic length scale. In fact, 19 out of the 26 data points (or about 73%) showed the drop while spinning sample creating a larger length scale than the 5 second exposure time. A possible explanation for this result is that the 'drop while spinning' solvents have less time on the sample surface before evaporating after spinning begins.

Another conclusion of note is that the lateral length scale tends to be solvent-independent. That is, the length scale qualitatively follows the same trend independent of what solvent the surface was exposed to. All of the solvents utilized in experiments were considered poor solvents for polystyrene but differed in chain length. That, however, seems to not have an effect of the length scale of the resultant roughness. The reasoning behind this result remains unclear.

The final remark to be made regarding the plot is that all of the characteristic length scales range between 20 nm and 180 nm. Therefore, the effect of a poor solvent on the surface of a polymer thin film is certainly nanoscopic in region size. This is of particular importance as many nanoscale manufacturing techniques such as nanolithography and etching occur on the same scale as the morphology examined here.

3.3.2 Morphology Amplitude

The combined results for the bump amplitude of the solvent-induced morphology are shown in Figure 3.10. All of the samples used for the amplitude experiment were a 5 second exposure time and a 2 μm AFM image size.

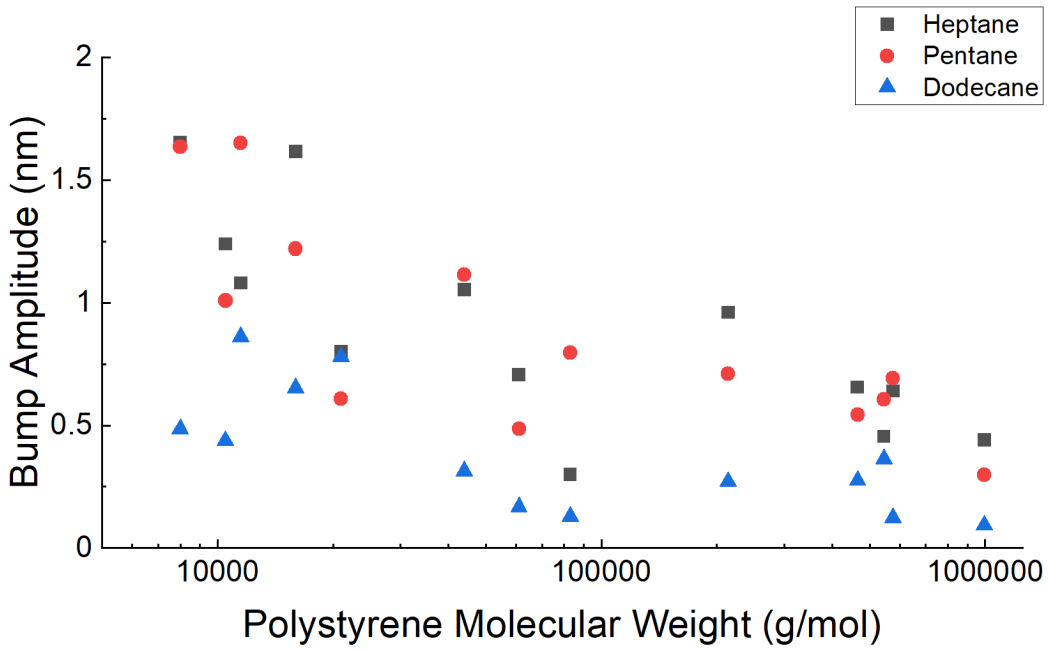

Figure 3.10: Plot of nanoscopic morphology amplitude as a function of molecular weight and solvent. The x-axis follows a logarithmic scale. Error bars were calculated but were left off the plot for increased visual interpretation.

From Figure 3.10, the following results can be extracted. First, it is clear that there exists a relationship between nanoscopic bump amplitude and polymer molecular weight. There is not a conclusive fit to the plot but the relation is approximately an exponential decay where larger amplitudes correspond to smaller molecular weights. This result is clear as smaller molecular weights are more easily dissolved than longer chains, resulting in a "rougher" surface.

Another conclusion is that the morphology induced by dodecane is significantly smaller than that of the other two solvents. This result is most likely related to vapour pressure and the solvent evaporation rate. The vapour pressure of dodecane is orders of magnitude smaller than that of pentane or heptane, meaning that it evaporates extremely slowly

compared to the other solvents and does not get quenched as quickly. It is currently unclear how this mechanism works but it seems that both solvent quality and vapour pressure play a part in the resultant bump amplitude.

A final observation is that all of the bump amplitudes range between 0.1 nm and 1.7 nm. Similar to the length scale results, the morphology amplitude exists on the scale of nanoscopic engineering techniques.

As an extension of the PS experiments, similar studies were completed on PMMA such that results can be generalized to a wider range of polymers. As this was a proof of concept experiment, only two molecular weights of PMMA were used; one below and one above the entanglement molecular weight.

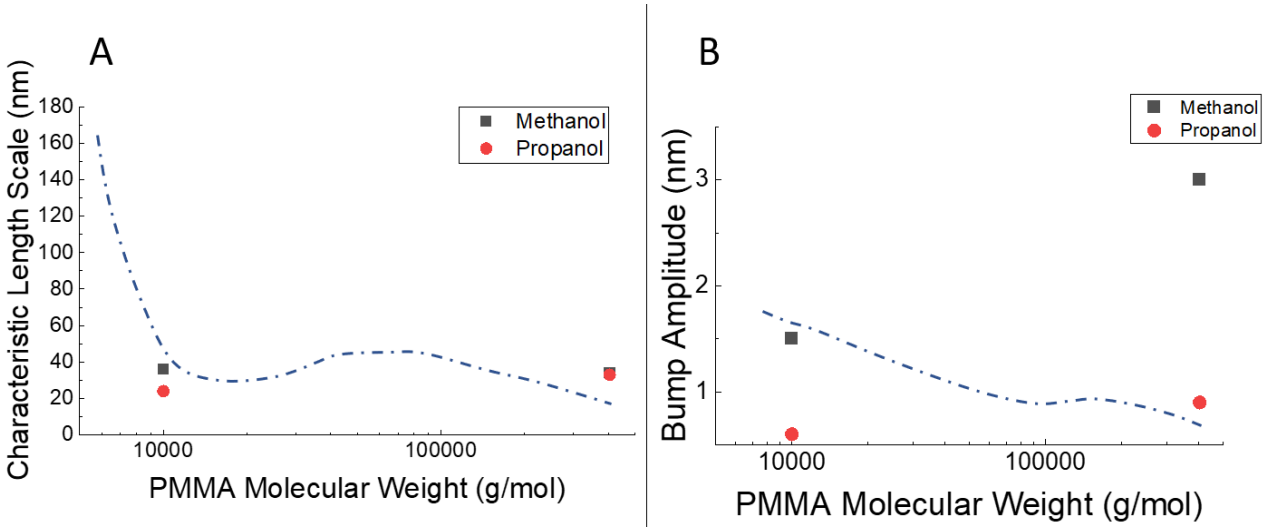

Figure 3.11: Characteristic length scale of PMMA as a function of molecular weight and solvent (A) and the nanoscopic bump amplitude of PMMA as a function of molecular weight and solvent (B). Both plots show a blue dashed overlay of the comparable plot for PS and both horizontal axes follow a logarithmic scale.

It can be seen from Figure 3.11 that a solvent-induced morphology is present for PMMA in a similar manner as that of PS. From the two data points it is unclear whether the trend follows that of PS. The main result to garner here is that a nanoscopic length scale and bump amplitude occur due to poor solvents on the PMMA surface and are of the same order of magnitude as PS.

3.3.3 QCM Swelling

A final analysis of the solvent-polymer system was completed with QCM-D, as described in Chapter 2. The results for each test system are summarized in Figure 3.12.

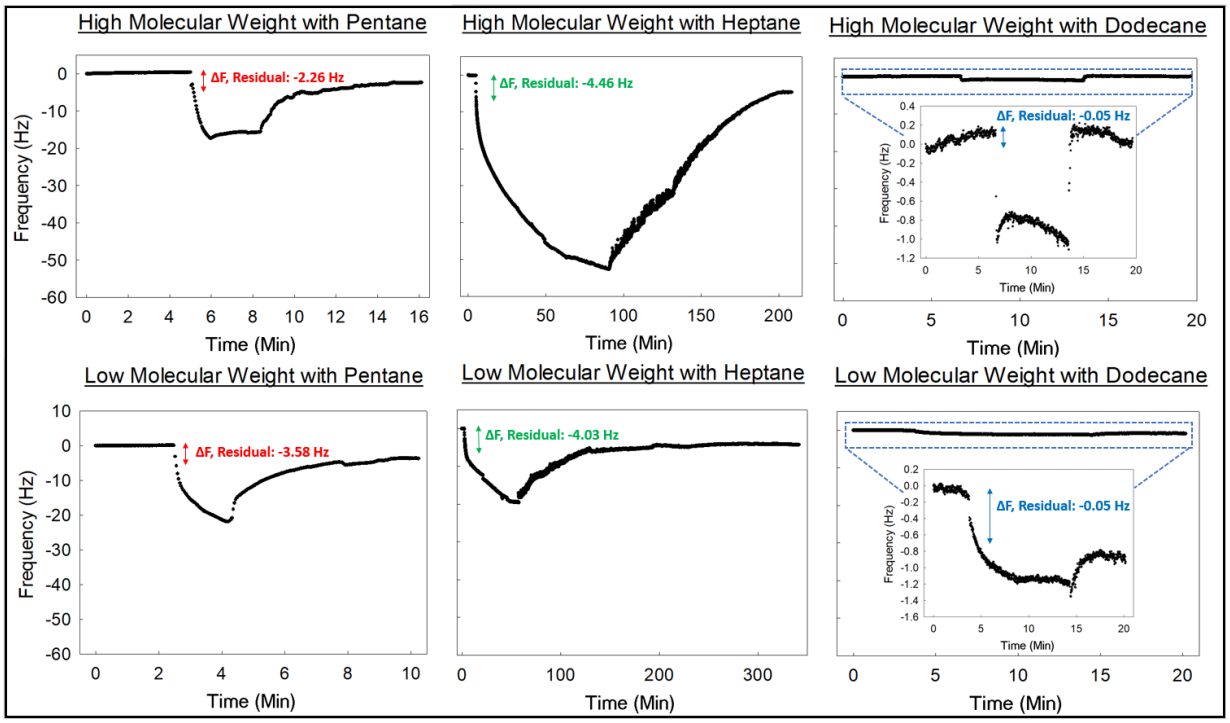

Figure 3.12: Plots of QCM-D frequency change as a function of time. High M_w (545000 g/mol) PS samples are shown on the upper row while low M_w (8000 g/mol) are below. At small times, a horizontal line is seen as the baseline frequency for the sample. When the frequency dips, solvent has been added and is swelling the surface. At the bottom of the well, a brief equilibrium in frequency is seen as the surface is fully swollen by vapour. The frequency recovers when the vapour is allowed to escape the system. A flat line is seen at large times as the 'new' equilibrium value for the system. The difference in beginning and final equilibrium (ΔF, Residual) corresponds to the amount of solvent the polymer retains after the swelling process.

The QCM-D data shows the mass of solvent remaining in the system after the polymer thin film has been swollen, then allowed to evaporate. The remaining solvent corresponds to the nanoscopic morphology present on the surface of the films after exposure to poor solvents. This technique allows for determination of whether the morphology effects occur

in the surface or bulk region of a polymer thin film. Shown in Table 3.1 are the pertinent values of remaining solvent mass for each system, as calculated through the Sauerbrey equation.

M_w (g/mol)	Solvent	Residual Frequency (Hz)	Remaining Mass (ng/cm^2)
545000	Pentane	-2.26	40
545000	Heptane	-4.46	78.94
545000	Dodecane	-0.05	0.885
8000	Pentane	-3.58	63.37
8000	Heptane	-4.03	71.33
8000	Dodecane	-0.05	0.885

Table 3.1: Relation of PS molecular weight and solvent type to the residual solvent mass in a polymer thin film system after swelling.

The main result that is shown in Figure 3.12 and Table 3.1 is the amount of solvent retained between the different solvents. In all cases, heptane shows the largest mass retention and dodecane the smallest. This result could be indicative of solvent quality. This conclusion also leads to the idea that differing poor solvents will contribute in varying manners towards the thickness of the solvent-rich layer versus the polymer-rich layer on the thin film surface.

As an extension to the QCM results, a loose calculation was completed to determine the approximate height of the swollen layer. Perlich *et al.* suggest that $\approx 10\%$ of the solvent is remaining in the film when it is swollen (discussed in further detail in Chapter 4)[20]. From there, it can be approximated that polystyrene has a density similar to water, 1 g/cm^3. Further, recall that the mass change (Δm) is a mass per unit area. Then, the calculation for layer height, while remembering to convert units between the QCM results and the polymer density, is

$$H = \frac{10 \times \Delta m}{\rho} \tag{3.6}$$

where H is the height of the swollen layer and ρ is the approximate polymer density. The results are shown in Table 3.2.

M_w (g/mol)	Solvent	Remaining Mass (ng/cm^2)	Swollen Layer Height (nm)
545000	Pentane	40	4.0
545000	Heptane	78.94	7.9
545000	Dodecane	0.885	0.09
8000	Pentane	63.37	6.4
8000	Heptane	71.33	7.1
8000	Dodecane	0.885	0.09

Table 3.2: Relation of PS molecular weight and solvent type to the approximate swollen layer height.

It is clear from both Table 3.1 and Table 3.2 that the remaining mass and height of the swollen layer is significantly less for dodecane than for pentane or heptane, suggesting that it may be an inferior solvent for PS.

Chapter 4

Discussion

In this chapter, a brief literature review will be completed with the purpose of providing a physical explanation as to the experimental results I obtained. Then, I will propose my own combined model and compare my results to the literature.

4.1 Comparisons to Polymer Brush Models

Based on previous work that has been completed in the area of solvent-induced morphology, it becomes important to compare the results from this thesis to theories in the literature. While various work has been completed in this area (see section 1.5), no single theory can fully describe the behavior that is shown through the work of this thesis. Therefore, it is pertinent to combine various theoretical models with previously-examined systems and relate them to my experimental results. The goal here is to present a cohesive understanding of the physical mechanism which leads to the nanoscopic morphology on polymer thin films when exposed to poor solvents. At the time of writing this thesis, the best theoretical overview of the mechanism involves the swelling of polymer chains by a poor solvent, grafted polymer chains, and domain separation upon chain collapse due to lateral instabilities. All of the theories relate to polymer brushes, so an analogy to brushes will be focused on. In the following sections each portion of the overall system explanation will be examined in further detail with the hope of providing a cohesive comparison. Summarily, the proposed model will be discussed in full and compared with the current literature.

4.1.1 Swollen Chains & Phase Separation

In a polymer-solvent system where the solvent is of poor quality, the interaction between monomers is preferred to the interaction of monomers to solvent particles[56]. However, when the thin film is introduced to solvent in either vapour or liquid form at a high rate, mass uptake (swelling) will occur until the thermodynamic equilibrium of the system is reached[57, 58]. If solvent is added after the equilibrium point, the system will reach a critical point, or θ point, where the system may phase separate[59, 15].

In the QCM-D experiments completed for this thesis, solvent vapour was added as shown by the mass change of the system but subsequently was removed before the critical point as the system never reached the θ temperature. In a situation like this, it is known that the swollen chains will completely collapse after the poor solvent has been removed. Furthermore, the system will often form domains or phase-separated regions due to the collapse of chains[60]. The theory behind this behavior is best described by the work of Chan *et al.*[61]. Based on the theory of Cahn and Hilliard it is known that, when quenched below its upper critical point, a binary solution of polymer and solvent will phase separate through spinodal decomposition[62]. The beginnings of the decomposition, or phase separation, are well described by the linear Cahn-Hilliard equation but the latter process should be represented by the nonlinear equation (introducing nonlinearities in the free energy) and requires a numeric solution[62, 61]. The Chan group provides a theory for the latter process of decomposition by applying a fourth order polynomial free energy to the nonlinear Cahn-Hilliard equation. Since the system is related to a solvent-polymer interaction, the Flory-Huggins free energy was chosen to be inputted. Through numeric simulation, it was found that spinodal decomposition in binary systems with poor solvent behave in one of two manners:

- If the system is quenched at its critical point, the phase separation that results from chain collapse acts like interconnected structures
- If the system is quenched prior to its critical point, the phase separation forms a droplet-type morphology

This theory of phase separation is compelling as a preliminary model for the work of this thesis as it describes a similar morphology resultant from solvents. However, it does not provide the full picture.

A second study by Perlich *et al.* furthers the idea that the work of this thesis is partially related to swelling[20]. The Perlich group completed a neutron reflectivity study

to determine the portion of solvent remaining in the surface layer of a polymer thin film after spin coating. While no comment was made regarding surface morphology, it was suggested that the solvent swells the polymer surface during the first stages of spinning.

Based on the previous studies examined here, it is then proposed that the system presented in this thesis is swollen when the poor solvent is introduced. However, the length scales shown in this thesis are significantly smaller ($\sim$ 20-100 nm) than those introduced solely by swelling phase separation ($\sim$ 2-20 μm)[60]. Further theories will be explored in the next section to provide a more complete description of the nanoscopic morphology that has been discovered experimentally.

4.1.2 Grafted Chains

In systems of polymer brushes, it is often the case that the polymer chains are chemically grafted onto a substrate by one of their ends. This results in a "brush" type structure when the chains are extended, however, there exists a second type of grafted chain which is less studied in the scientific literature. Two possible theories for these doubly-grafted chains are presented next.

Entanglement Grafts

When long polymer chains become entangled, as described in Chapter 1, they form a type of network whereby entanglement points restrict the motion of the monomers between them (Figure 4.1). In this case, a form of physical grafting can be presented as the chains are essentially immobile at the entanglement/grafting points[63].

It is possible, then, that a physical grafting mechanism is taking place with entanglement points as grafting nodes. This analogy would allow for swelling and stretching of polymer chains between entanglement points while being restricted to the physical grafts. In this description, a poor solvent could swell the chains and lead to a minor phase separation where clusters of polymer "rich" zones and polymer "poor" zones could exist within the grafting framework. It is important to note that this proposed model has possible downfalls. It is known that polymers are almost entirely made up of intra-entanglement near the surface of the film while the bulk shows inter-entanglement which introduces further complication to the proposed theory[63]. Regardless of this uncertainty, the model remains sufficient to provide a general description of what was viewed experimentally and will continue to be utilized.

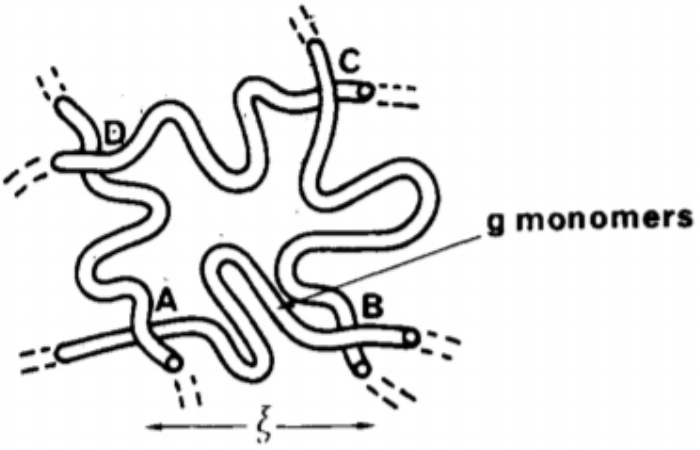

Figure 4.1: An entangled polymer network. Points A,B,C, and D act as physical grafting points while the length ξ shows the distance between said points. Image taken from[64].

Swollen Grafts

An alternative explanation for the formation of doubly-grafted chains is that of a solvent penetration plane. When the polymer chains are exposed to a solvent, they will swell as shown by the QCM data in Figure 3.12. Then, there will be regions of chains which exist in the swollen layer as it collapses thereby forming a grouped morphology. This is represented in the work by Perlich *et al.* where it can be extrapolated from their plot that about 10% of poor solvent remains in the free surface at the relevant M_w, even after collapse and evaporation (Figure 4.2)[20]. It is, therefore, a reasonable assumption that the grafting points may be related to chains entering and leaving the remaining solvent region of the film. It is important to note that this reasoning will not be carried forward for the purpose of providing a model, as it is a secondary explanation.

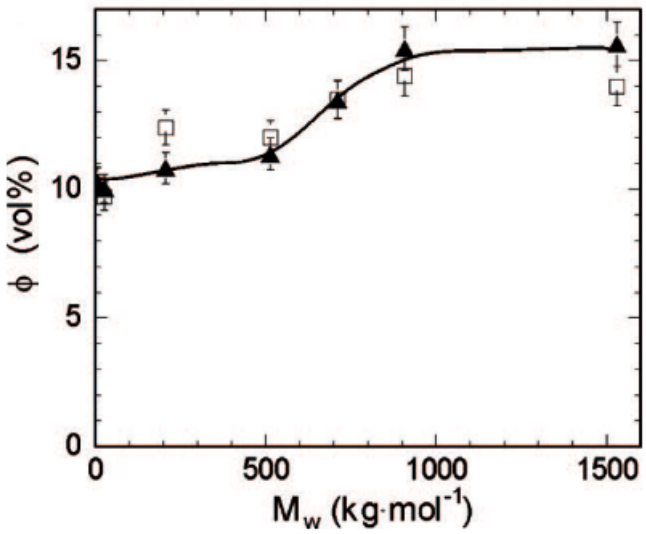

Figure 4.2: Neutron reflectometry measurement of remaining solvent (deuterated toluene) in PS thin films as a function of molecular weight. Note the molecular weight unit is kg/mol, rather than g/mol when being compared with the work of this thesis. Image adapted from [20].

4.1.3 Lateral Instabilities & Length Scale

Based on the explanation of experimental findings up until this point, there remains an unknown piece of the model which explains the existence of a characteristic length scale. To provide this final portion, the theory of lateral instability will be presented.

Some of the early investigations into lateral instability of collapsed chains came from Halperin in 1988 and Zhulina *et al.* in 1987[18, 65]. Both studies presented theoretical calculations regarding the collapse of grafted chains in poor solvents. Halperin used a mean field theory approach and found that, for low surface grafting density, the chain collapse is associated with a first order phase transition[18]. Zhulina *et al.* employed an average field approximation and found that the grafting density of the collapsed units decreased with decreasing solvent quality (while all solvents still remained in the poor solvent regime)[65]. Both of these early studies calculated the conformational free energy of chains within the

system as

$$\frac{F}{kT} = F_{el} + F_{mix} \tag{4.1}$$

where F_{el} describes the elastic, or stretching, contribution of the chains by the solvent swell and F_{mix} describes the interaction between the grafts and the chains, and k represents the Boltzmann constant. Then, by minimizing the total free energy with respect to the radius of a grafted bunch, it was concluded that the regions would be of radius $R \sim N^{3/5}$[18]. It should be noted that a scaling of $N^{3/5}$ represents a polymer in a good solvent. This is an unexpected result as this theory dealt with poor solvents specifically. Therefore, this work is likely not ideal to describe the morphology seen in this thesis.

The next set of studies that elaborated upon the theoretical framework of lateral instability in grafted chain were completed simultaneously in 1992 by Ross & Pincus and Lai & Binder[66, 67]. Both studies relied heavily on statistical mechanics and mathematics and, therefore, will not be examined in great depth. It is still important to recognize that both of these studies are seminal in the field and provided a strong base for those that came after. The work by Lai & Binder utilized Monte Carlo simulations near the θ point with a bond fluctuation model. Indeed, the study discovered that there existed a lateral instability in the grafted region upon collapse below the θ point of the system[66]. Ross & Pincus applied a random phase approximation and found that there exists an instability similar to that found by Lai & Binder but suggested that it indicates spinodal decomposition. Further, Ross & Pincus provided a rough characterization, stating that the mean graft spacing should be significantly smaller than the radius of gyration of the polymer[67]. In the years following these works other authors completed similar studies, all of which confirmed the formation of chain groups upon collapse[68, 54, 69].

A paper on lateral instability was published by Williams in 1993[19]. This work has since been cited extensively in describing the collapse of grafted chains due to poor solvents. Williams also coined the term "micelles" to describe the polymer-rich regions which form after the chain collapses. The theory focused on free energy, which leads to a scaling law for the size of the micelles. First, in a bad solvent, monomers will minimize the undesirable contact with the solvent by forming a micelle. However, this formation comes with an energy penalty of

$$F_{pen} = kT\frac{R_\theta^2}{R^2} \tag{4.2}$$

where $R \sim bN^{1/3}$ scales like chains in a poor solvent and $R_\theta \sim bN^{1/2}$ scales like chains in a theta solvent, representing a surface energy term. From this, the theta term dominates the free energy and the swollen chains will form micelles once collapsed due to the lesser

penalty of that behaviour in poor solvents. The pictorial idea of the micelles is shown in Figure 4.3.

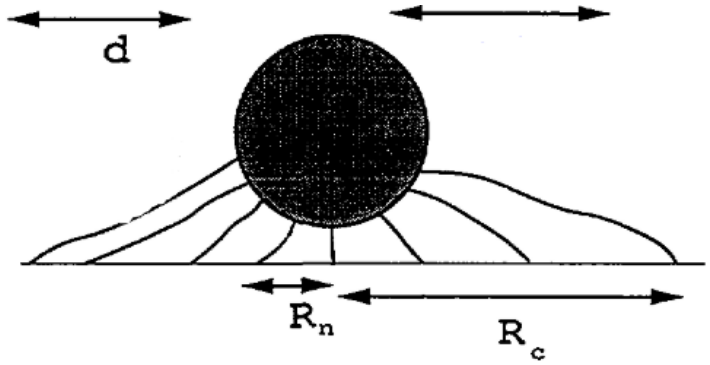

Figure 4.3: A depiction of a polymer chain "micelle". The chains of radius R_c will collapse to form micelles of radius R_n with the distance between micelles, d, relating to the characteristic length scale of the surface morphology Image adapted from [19].

To determine the characteristic micelle size, Williams followed a free energy model similar to previous studies, with a stretching and entropic component.

$$F \sim \left(\frac{\rho}{b}\right) R_c + \left(R_c^2 \rho N\right)^{2/3} R_c^{-2} \tag{4.3}$$

Williams found the free energy system to have a minimum at the micelle size of

$$R_c = bN^{2/5}(\rho b^2)^{-1/5} \tag{4.4}$$

with $n = N^{4/5}(\rho b^2)^{3/5}$ chains per micelle. Therefore, this work provides a theoretical model which calculates the micelle size[19]. A point of note is that Williams theory is dependent on the micelle being grafted to the substrate surface. Therefore, there exists a repulsive interaction between the surface and the monomers, thereby creating a stretching energy. This is not the case of the current thesis work as the grafted chains exist solely in the free surface of the polymer film and have a favourable interaction between polymer chains.

As an alternative theory to that of Williams, Yeung *et al.* published a theoretical work regarding a similar system in the same year[54]. The researchers applied a random phase approximation theory along with a numeric mean-field model to determine the lateral instabilities for polymers in a poor solvent. It was found that, for large N, the mean-field solution becomes unstable tangential to the grafting plane. In this particular lateral instability, the polymers were found to group into clumps and create a "dimpled" surface

(Figure 4.4). In this theory, the polymer ends are only "grafted" so far as they form groupings which create a surface morphology. Therefore, this theory may be more compelling to describe the results found in this thesis than that of Williams.

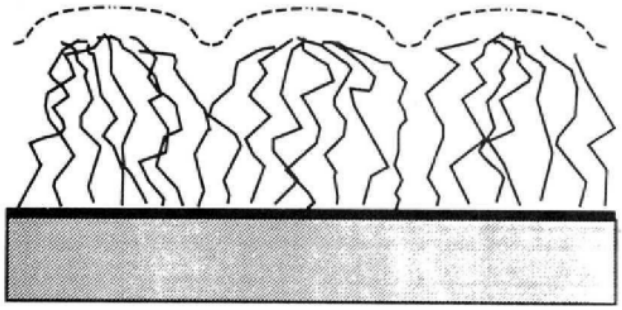

Figure 4.4: A depiction of the "dimpled" grafted regions proposed by Yeung *et al.* Image taken from [54].

After the works by Yeung and Williams, multiple experimental studies were completed to test the lateral instability theory. In 1994, Zhao *et al.* compiled an AFM study on grafted PS[70]. The group exposed a PS thin film to a good solvent, toluene, that was flowed over the surface in small amounts and over short time periods. The resultant micelle-type clusters were ≈100 nm in radius and had heights of 10 nm. It was also found that the resultant morphology showed a 1% grafting density on the surface[70]. Another AFM study was completed in 1996 by Stamouli *et al.* where a diblock co-polymer was used to create a thin film and was subsequently exposed to poor solvent[71]. The resultant morphology is very similar to that found in the work of this thesis. The bunches in this study were found to have a height of ≈14 nm and radii of ≈ 19 nm[71]. Another study completed by Koutsos *et al.* used scanning force microscopy and determined a very similar result[72]. The clusters in this case were shown to have a height of ≈6 nm and a radius of 24 nm. Further, the Koutsos paper also presented a scaling argument regarding the grafting density of the chains. It was suggested that the diameter of the bunched groups scaled as $d \sim N^{2/5}\rho^{-1/5}$, which is in perfect agreement with the previous work by Williams[72, 19]. These experimental studies show results strikingly similar to that of this thesis in the way of morphological amplitudes and characteristic length scales. This provides promising confirmation that the lateral instability must be added to the swollen grafted chain model that is being built up in this chapter.

More recently, the idea of lateral instability has, once again, been investigated. This final group of papers combine the theoretical and experimental work with modern simula-

tions, leading to very convincing results which may provide a theory of the work herein. Jentzsch & Sommer provided molecular dynamics simulations using a bond fluctuation model to investigate lateral instabilities while varying the grafting density, solvent quality, and chain length within the model[73]. Further, this paper included entanglement effects and the results agreed with Williams free energy theory of the micelles. In 2015, Lappala *et al.* completed a different molecular dynamics simulation that was based upon coarse-grained Brownian dynamics with a swell and collapse behaviour[74]. Once again, the system agreed with previous results. As a final exploration of a paper, in 2017, Brettman *et al.* created a micelle model for polyelectrolyte brushes in the presence of multivalent ions[75]. While this investigation is obviously of a different system, the resultant morphology is strikingly similar to that seen in this thesis. At low grafting density, the formation of micelles was seen while at high grafting densities, a uniform layer was formed. The model by Brettman *et al.* found an equilibrium height of the morphology to be 5.3 nm, though it is important to note that the height corresponds to a singly-grafted polymer brush while this thesis employs doubly-grafted entanglement networks[75]. Through the investigation of numerous theoretical and experimental models as well as simulations, it is safe to state that a lateral instability most likely occurs as the third portion of the explanation for the surface morphology presented in this thesis work.

4.2 Proposed Model & Validation

Through determining and describing the various physics that take part in creating the nanoscopic morphology seen in this report, I propose a cohesive model of the physical mechanisms driving poor solvent-induced nanoscopic morphology of polymer thin films. It is important to note that this model is an approximation for the exact physics behind the experimental findings of this thesis. An overview is presented here, as follows. First, when a polymer solution is deposited onto the silicon substrate, so long as its M_w is sufficiently large (above the entanglement M_e), it creates a network-like structure where physical grafts are realized by entanglement points or a solvent-swollen layer. Then, when a poor solvent is introduced to the system below the θ temperature, a subsequent swell of the polymer chains will commence. Since the system cannot fully saturate with solvent, it will reach a sub-critical point whereby a phase separation occurs. At this point, the free energy of the system undergoes a competition whereby the grafted chains attempt to stretch and swell while the entropy of mixing shows a congregation of chains into bunched regions. Specifically, the energetics of the system show a preference for forming compact bunches as there is an unfavourable interaction between the monomers and the poor solvent

molecules. However, the entropy would prefer a more elongated chain as the ideal chain scaling is $\sim N^{1/2}$ and there exists an entropy cost for a more compact state in poor solvents of $\sim N^{1/3}$. This energy-entropy competition of terms is unable to reach a fully equilibrated state thereby developing a lateral instability which causes the system to form a morphology. Finally, the system undergoes a quench as the solvent vapour leaves the polymer and the polymer-rich and polymer-poor zones are deflated onto the substrate surface.

In order to provide a full analysis of the experimental system, a three-dimensional random walk simulation was completed. The random walk was simple and did not include self-avoidance and, as such, should be taken as an approximation of the system. The simulation was allowed to walk freely in the x and y-directions with each step set to be a Kuhn length of PS. However, in the z-direction, a variable reflecting boundary condition was set to model the physical top boundary of the PS thin film. Then, the simulation was set to walk infinitely until manually stopped. For the full simulation, approximately 500,000,000 steps were completed. The python script would keep track of the chains that walked into the free surface from below (enter z=0 plane) and back out of the free surface (cross back below z=0) without solely walking along the z=0 plane. These chains were considered to be "grafted chains". An example of the simulation is shown in Figure 4.5.

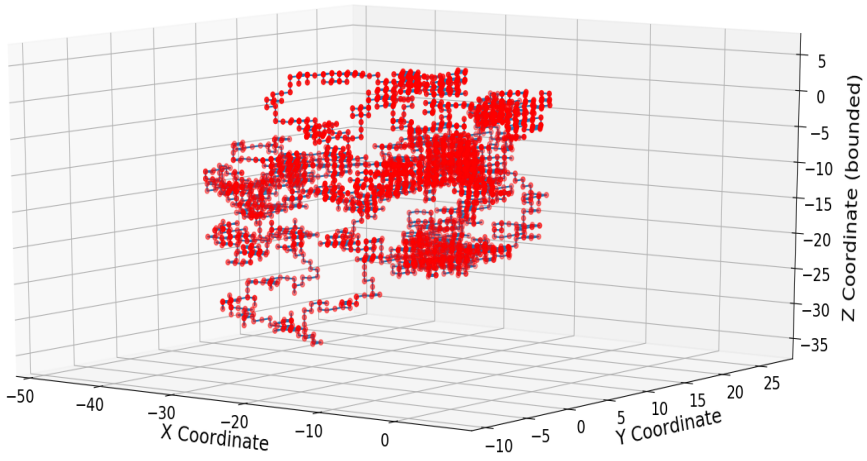

Figure 4.5: A visual output of the 3-dimensional random walk simulation. In this case the upper boundary, z^*, is set to be 5 Kuhn lengths. This simulation consisted of 35,000 steps and is only used for depiction purposes as it is too small for valid calculations.

To ensure the validity of the computer-simulated walk, a theoretical calculation of the percentage of walks, z, which enter the $0 < z < z^*$ region and subsequently walk back out. This percentage, P_{graft}, represents the number of walks which become grafted as opposed to those that remain in the bulk and can be evaluated as a geometric sum, as follows:

$$P_{graft} = \frac{1}{6} + \frac{1}{6}\sum_{n=1}^{\infty}\left(\frac{4}{6}\right)^n$$

$$P_{graft} = \frac{1}{6}\sum_{n=0}^{\infty}\left(\frac{4}{6}\right)^n$$

$$P_{graft} = 0.5 = 50\% \tag{4.5}$$

From the simulation, averages of grafted chains were calculated and fell distinctly in the expected range, with values between 49.2% and 50.6% across the range of z^*. Thus, the simulation was taken to be a good approximation of the experimental system.

Once the simulation was tested to be functioning as expected, values were extracted from a lengthy simulation and plotted to determine a distribution of grafted chain lengths. The output plot is shown in Figure 4.6.

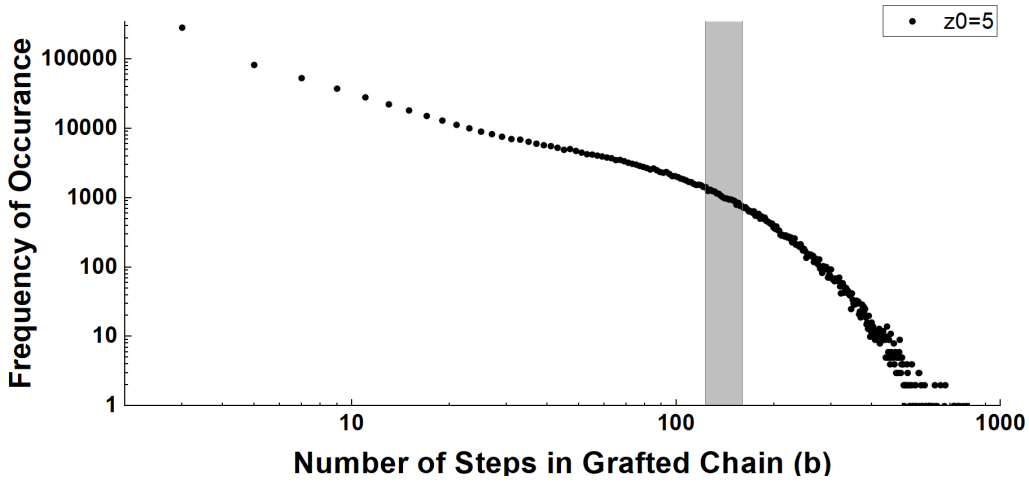

Figure 4.6: A distribution of grafted chain lengths in units of Kuhn steps, b. This distribution was completed for $z^* = 5$. The grey overlay represents the range of entanglement lengths for PS.

The information from Figure 4.6 provides valuable comparison with literature. First, the grafting density of the simulation can be calculated. To do this, the number of grafted chains with steps larger than entanglement (above $N_e = 180$) were taken as a percentage of the total sum of grafted chain lengths in the simulation. Based on the model that the entanglement points are acting as grafting points, the grafting density is calculated to be 2.05%. This value is comparable to studies that were previously introduced, with Jentzsch & Sommer stating grafting densities which ranged from 1%-2.4% and Zhao *et al.* showing densities of 1%[73, 70]. Further, the simulation output can be worked backwards to confirm the model of entanglement grafting points. This is seen as, in Figure 4.6, the plot begins to drop off into a steep decline at $\approx N = 100$. Seeing as the change in regime occurs at the upper end of the entanglement range for PS, it follows that the grafting density relates to the entanglement points.

Other comparisons that are important to make are qualitative analyses of experiments from this thesis and their relation to the literature values. First, the amplitude of the experimental morphology should be recalled. Based on AFM measurements, the surface roughness seen in this thesis ranges between 0.2 nm and 1.8 nm. Brettman *et al.* found an equilibrium brush height of 5.3 nm while Koutsos *et al.* found a height of 5.5 nm[75, 72]. Both of these literature studies, however, were examining polymer brushes which were only single-end grafted. That is, if those brushes were doubled-over, their amplitudes would be halved and they would be on the correct order to compare to the experimental results of this thesis. This suggests that the literature theory aligns with the model proposed here and that the work of this thesis is reasonably accurate.

The final comparison to complete is that of characteristic length scale of the solvent-induced morphology. As reviewed in the previous sections, most of the literature agrees that the polymer bunches' characteristic scale has a dependence which scales like $\sim N^{2/5}$[19, 72, 18]. While it is difficult to directly compare the length scale of this work to the literature, seeing as the scaling law would only apply above the entanglement region according to the proposed model, a quantitative measurement may still be made. In the theory by Williams, a characteristic radius of the micelles is told to be

$$R_c = N^{2/5}\rho^{-1/5}b^{3/5} \tag{4.6}$$

where b is the Kuhn length (1.8 nm for PS). If the grafting density calculated from the random walk simulation is assumed to be correct, then the characteristic length of this research can be calculated as

$$R_c = (180)^{2/5}(0.02\ \text{nm}^{-2})^{-1/5}(1.8\ \text{nm})^{3/5}$$
$$R_c = 24.8\ \text{nm}$$

If the characteristic radius should theoretically be 24.8 nm, then the characteristic length scale (distance between surface features) should be $D_c = 2R_c = 49.6$ nm. According the Figure 3.9, the experimental length scale at the point of PS entanglement is ≈ 40 nm. The similarity between theory and experiment is extremely promising in the case of characteristic length.

The comparisons between simulation, theory, and experiment presented in this chapter all provide support to the model proposed for the work of this thesis and suggest that the work completed does, indeed, show a novel mechanism in the area of polymer nanophysics. The reader is reminded that the model presented in this discussion is not comprehensive. There exists debate as to the physical mechanism between the "grafted" chains and it is not concrete whether the morphology present in this work can be directly related to polymer bushes.

Chapter 5

Conclusion

This chapter will provide a brief summary of the work completed in this thesis. I will also present technological applications of my work.

5.1 Summary of Work

In conclusion, this thesis presents experimental findings related to poor solvent-induced nanoscopic morphology as well as a proposed model to explain the underlying physics. Experimental characterization techniques such as atomic force microscopy and quartz crystal microbalance were utilized to examine the surface features of polymer thin films. Mathematical methods, such as the radial power spectral density function, were then applied to determine the length scales and nanoscopic roughness of the morphology. Finally, statistical mechanics and polymer random walk simulations were applied to determine a theoretical basis for an explanation of the results.

In this work, it was found that a surface morphology is present on polymer thin films due to the presence of a poor solvent. Solvents of this quality were previously thought to have no lasting effect on the surface but this work proves otherwise. It was found that nanoscopic bumps were formed on both PS and PMMA after evaporation of a poor solvent and showed a characteristic length scale across the surface of approximately 40 nm. The bumps were investigated with atomic force microscopy and showed roughness amplitudes on the thin film surface on the order of 2 nm. These results were further confirmed by the use of quartz crystal microbalance which showed that residual solvent was present in the polymer films even after evaporation and wait times upwards of 24 hours.

A 3-dimensional random walk simulation with a reflecting boundary surface was created for this work to aid in the comparison of experimental results to theoretical work in the literature. The results directly aligned with the experimental results of this thesis. Further, numerous reports from the scientific literature were collected and analyzed; a significant portion of which confirmed my experimental findings.

Finally, a physical model was proposed to describe the mechanism driving the nanoscopic morphology. A combination of solvent swelling, phase separation of grafted polymer chains, and energy-entropy competitive lateral instability were presented. While the proposed theory is not comprehensive, it has been shown to provide a general understanding of the systems at hand.

5.2 Relevant Applications

Polymer thin films are widely used across the scientific community to create devices or state-of-the-art technology. Tuning the surface properties of such materials can often optimize or enhance the output, meaning that surface morphology has great impact on various applications. Relevant fields or applications that may use the information presented in this thesis include nanolithography or wet etching for the purpose of nanoelectronics, micro-devices for use in solar cells, targeted drug-delivery systems, organic transistors, and more[74, 14, 76]. In the creation of said devices, I suggest that researchers use caution when applying poor solvents to their polymer surfaces as it may cause an unexpected result.

Bibliography

[1] Michael Rubenstein and Ralph H. Colby. "Polymer Physics". In: (2003).

[2] *Polymer - the classification collection*. URL: https://europlas.com.vn/polymer-means-many-monomers/ (visited on 08/12/2020).

[3] David I. Bower. "An Introduction to Polymer Physics". In: (2002).

[4] Paul C. Painter and Michael M. Coleman. "Fundamentals of Polymer Science". In: (2000).

[5] Ulf W. Gedde. "Polymer Physics". In: (1999).

[6] P.G. De Gennes. "Scaling Concepts in Polymer Physics". In: (1979).

[7] Gert Strobl. "The Physics of Polymers". In: (1997).

[8] *Random Walks*. URL: https://www.mit.edu/%7B~%7Dkardar/teaching/projects/chemotaxis(AndreaSchmidt)/random.htm (visited on 08/10/2020).

[9] Chinedum Osuji. *Lecture Notes: ENAS 606 : Polymer Physics*. 2017. URL: https://www.eng.yale.edu/polymers/docs/classes/polyphys/lecture%7B%5C_%7Dnotes/3/handout3.pdf.

[10] Stuart A Mcnelles et al. "Quantitative Characterization of the Molecular Dimensions of Flexible Dendritic Macromolecules in Solution by Pyrene Excimer Fluorescence". In: *Macromolecules* 51 (2018).

[11] Masao Doi and S Edwards. "The Theory of Polymer Dynamics". In: (1986).

[12] Alexei E. Likhtman and M. Ponmurugan. "Microscopic definition of polymer entanglements". In: *Macromolecules* 47.4 (2014), pp. 1470–1481. URL: https://pubs.acs.org/sharingguidelines.

[13] *Products formerly Ice Lake*. URL: https://ark.intel.com/content/www/us/en/ark/products/codename/74979/ice-lake.html (visited on 07/21/2020).

[14] Antonia Statt, Michael P. Howard, and Athanassios Z. Panagiotopoulos. "Solvent quality influences surface structure of glassy polymer thin films after evaporation". In: *Journal of Chemical Physics* 147.18 (2017).

[15] Paul Flory. "Thermodynamics of high polymer solutions". In: *Journal of Chemical Physics* 22.4 (1941), pp. 415–426.

[16] Maurice L. Huggins. "Thermodynamic Properties of Solutions of Long-Chain Compounds". In: *Annals of the New York Academy of Sciences* 43.1 (1942), pp. 1–32.

[17] *Flory-Huggins theory page - Statistical mechanics and thermodynamics*. URL: http://www.sklogwiki.org/SklogWiki/index.php/Flory-Huggins%7B%5C_%7Dtheory (visited on 08/14/2020).

[18] A. Halperin. "Collapse of Grafted Chains in Poor Solvents." In: *Journal de physique Paris* 49.3 (1988), pp. 547–550.

[19] D Williams. "Grafted polymers in bad solvents: octopus surface micelles". In: *Journal de Physique II* 3.9 (1993).

[20] J. Perlich et al. "Solvent content in thin spin-coated polystyrene homopolymer films". In: *Macromolecules* 42.1 (2009), pp. 337–344.

[21] Hans Jürgen Butt. "Capillary forces: Influence of roughness and heterogeneity". In: *Langmuir* 24.9 (2008), pp. 4715–4721.

[22] Parvaneh Mokarian-Tabari. *Controlling the Morphology of Spin coated Polymer Blend Films*. Tech. rep. 2009.

[23] Günter Reiter. "Unstable Thin Polymer Films: Rupture and Dewetting Processes". In: *Langmuir* 9.5 (1993), pp. 1344–1351.

[24] H Richardson et al. "Structural relaxation of spin-cast glassy polymer thin films as a possible factor in dewetting". In: *Eur. Phys. J. E* 12 (2003), pp. 437–441.

[25] A. S. Kuznetsov, M. A. Gleeson, and F. Bijkerk. "Hydrogen-induced blistering mechanisms in thin film coatings". In: *Journal of Physics Condensed Matter* 24.5 (2012).

[26] P G De Gennes. "Solvent evaporation of spin cast films: "crust" effects". In: *Eur. Phys. J. E* 7 (2002), pp. 31–34.

[27] A. Karim et al. "Phase-separation-induced surface patterns in thin polymer blend films". In: *Macromolecules* 31.3 (1998), pp. 857–862.

[28] Longjian Xue, Jilin Zhang, and Yanchun Han. "Phase separation induced ordered patterns in thin polymer blend films". In: *Progress in Polymer Science* 37 (2012), pp. 564–594.

[29] Kenneth E. Strawhecker et al. *The critical role of solvent evaporation on the roughness of spin-cast polymer films*. 2001.

[30] Paul D. Fowler et al. "Controlling Marangoni-induced instabilities in spin-cast polymer films: How to prepare uniform films". In: *European Physical Journal E* 39.9 (2016), pp. 1–8.

[31] P. Müller-Buschbaum et al. "Solvent-induced surface morphology of thin polymer films". In: *Macromolecules* 34.5 (2001), pp. 1369–1375.

[32] Thomas G. Fox and Paul J. Flory. "Second-order transition temperatures and related properties of polystyrene. I. Influence of molecular weight". In: *Journal of Applied Physics* 21.6 (1950), p. 591.

[33] *Entanglement Spacing*. URL: http://polymerdatabase.com/polymer%20physics/Ne%20Table.html (visited on 08/16/2020).

[34] Nam-Trung Nguyen. "Micromixers - Fundamentals, Design and Fabrication". In: (2008).

[35] *Reflection and transmission at interfaces*. URL: https://www.researchgate.net/figure/Reflection-and-transmission-at-interfaces-a-Case-of-thin-film-on-substrate/ (visited on 08/14/2020).

[36] Mittleman. *Lecture Notes: Fresnel's Equations for Reflection and Transmission*. 2019. URL: https://www.brown.edu/research/labs/mittleman/sites/brown.edu.research.labs.mittleman/files/uploads/lecture13_0.pdf.

[37] Yongho Seo et al. "Real-time atomic force microscopy using mechanical resonator type scanner". In: *Reports on Progress in Physics* 79.10 (2008), p. 103703.

[38] *Atomic Force Microscopy - Nanoscience Instruments*. URL: https://www.nanoscience.com/techniques/atomic-force-microscopy/ (visited on 09/27/2019).

[39] *Atomic Force Microscopy (AFM)*. URL: https://warwick.ac.uk/fac/sci/physics/current/postgraduate/regs/mpagswarwick/ex5/techniques/structural/afm/ (visited on 09/27/2019).

[40] Nader Jalili and Karthik Laxminarayana. "A review of atomic force microscopy imaging systems: Application to molecular metrology and biological sciences". In: *Mechatronics* 14.8 (2004), pp. 907–945.

[41] R. Knoll, K. Magerle, and G. Krausch. "Tapping Mode atomic force microscopy on polymers: Where is the true sample surface?" In: *Macromolecules* 34.12 (2001), pp. 4159–4165.

[42] G. Bar et al. “Factors affecting the height and phase images in tapping mode atomic force microscopy. Study of phase-separated polymer blends of poly(ethene-co-styrene) and poly(2,6-dimethyl-1,4-phenylene oxide)”. In: *Langmuir* 13.14 (1997), pp. 3807–3812.

[43] *QCM-D — Measurements*. URL: https://www.biolinscientific.com/measurements/qcm-d (visited on 11/24/2019).

[44] Nagy L. Torad et al. “Advanced Nanoporous Material–Based QCM Devices: A New Horizon of Interfacial Mass Sensing Technology”. In: *Advanced Materials Interfaces* 6.20 (2019), p. 1900849.

[45] *Quartz Crystal Microbalance (QCM) - Nanoscience Instruments*. URL: https://www.nanoscience.com/techniques/quartz-crystal-microbalance/ (visited on 11/24/2019).

[46] John C. Russ and F. Brent Neal. “The Image Processing Handbook”. In: (2018).

[47] Takeshi Fujita and Ming Wei Chen. “Characteristic length scale of bicontinuous nanoporous structure by fast Fourier transform”. In: *Japanese Journal of Applied Physics* 47.2 (2008), pp. 1161–1163.

[48] Tevis D.B. Jacobs, Till Junge, and Lars Pastewka. “Quantitative characterization of surface topography using spectral analysis”. In: *Surface Topography: Metrology and Properties* 5.1 (2017).

[49] Zhaohui Yang et al. “Glass Transition Dynamics and”. In: *Science* 328 (2010), pp. 1676–1679.

[50] Hai Yao Deng et al. “Power spectral density of free-standing viscoelastic films by adiabatic approximation”. In: *Langmuir* 29.13 (2013), pp. 4283–4289.

[51] Zhaohui Yang et al. “Glass transition dynamics and surface mobility of entangled polystyrene films at equilibrium”. In: *Macromolecules* 44.20 (2011), pp. 8294–8300.

[52] Ophelia K.C. Tsui et al. “Equilibrium pathway of spin-coated polymer films”. In: *Macromolecules* 41.4 (2008), pp. 1465–1468.

[53] Ranxing Nancy Li et al. “Equilibration of polymer films cast from solutions with different solvent qualities”. In: *Macromolecules* 45.2 (2012), pp. 1085–1089.

[54] Chuck Yeung, Anna C. Balazs, and David Jasnow. “Lateral Instabilities in a Grafted Layer in a Poor Solvent”. In: *Macromolecules* 26.8 (1993), pp. 1914–1921.

[55] F. Y. Lin et al. “Measuring the solubility of solids in non-solvents: case of polystyrene in alkanes”. In: *European Physical Journal E* 39.10 (2016), pp. 1–5.

[56] Lukas Michalek et al. “Quantifying Solvent Effects on Polymer Surface Grafting”. In: *ACS Macro Letters* 8.7 (2019), pp. 800–805.

[57] Gabriel Bernardo and Drahosh Vesely. “Anomalous swelling of a polystyrene matrix in organic solvents”. In: *Journal of Applied Polymer Science* 115.4 (2010), pp. 2402–2408.

[58] Wojciech Ogieglo et al. “In situ ellipsometry studies on swelling of thin polymer films: A review”. In: *Progress in Polymer Science* 42 (2015), pp. 42–78.

[59] Rui Wang and Zhen Gang Wang. “Theory of polymer chains in poor solvent: Single-chain structure, solution thermodynamics, and θ point”. In: *Macromolecules* 47.12 (2014), pp. 4094–4102.

[60] H. R. Sheu, M. S. El-Aasser, and J. W. Vanderhoff. “Phase separation in polystyrene latex interpenetrating polymer networks”. In: *Journal of Polymer Science Part A: Polymer Chemistry* 28.3 (1990), pp. 629–651.

[61] Philip K. Chan and Alejandro D. Rey. “Computational analysis of spinodal decomposition dynamics in polymer solutions”. In: *Macromolecular Theory and Simulations* 4.5 (1995), pp. 873–899.

[62] John Cahn John W.; Hilliard. “Free energy of a nonuniform system. I. Free Energy of a Nonuniform System. I. Interfacial Free Energy”. In: *The Journal of Chemical Physics* 30.5 (1959), pp. 1121–1124.

[63] Lun Si et al. “Chain entanglement in thin freestanding polymer films”. In: *Physical Review Letters* 94.12 (2005).

[64] P. G. De Gennes. “Dynamics of Entangled Polymer Solutions. I. The Rouse Model”. In: *Macromolecules* 9.4 (1976), pp. 587–593.

[65] Ye B. Zhulina, V. A. Pryamitsyn, and O. V. Borisov. “Structure and conformational transitions in grafted polymer chain layers. A new theory”. In: *Polymer Science U.S.S.R.* 31.1 (1989), pp. 205–216.

[66] Pik-Yin Lai and Kurt Binder. “Structure and dynamics of polymer brushes near the &THgr; point: A Monte Carlo simulation”. In: *J. Chem. Phys* 97 (1992), p. 586.

[67] R. S. Ross and P. Pincus. “Bundles: End-grafted polymer layers in poor solvent”. In: *Journal de Physique II* 19.2 (1992), pp. 79–84.

[68] K. Soga, Hong Guo, and Martin Zuckermann. “Polymer Brushes in a Poor Solvent”. In: *EPL (Europhysics Letters)* 29 (July 2007), p. 531.

[69] Hai Tang and I. Szleifer. “Phase behavior of grafted polymers in poor solvents”. In: *EPL* 28.1 (1994), pp. 19–24.

[70] W. Zhao et al. “Lateral Structure of a Grafted Polymer Layer in a Poor Solvent”. In: *Macromolecules* 27.11 (1994), pp. 2933–2935.

[71] Amalia Stamouli et al. “An atomic force microscopy study on the transition from mushrooms to octopus surface ”micelles” by changing the solvent quality”. In: *Langmuir* 12.13 (1996), pp. 3221–3224.

[72] V. Koutsos et al. “Structure of chemically end-grafted polymer chains studied by scanning force microscopy in bad-solvent conditions”. In: *Macromolecules* 30.16 (1997), pp. 4719–4726.

[73] Christoph Jentzsch and Jens-Uwe Sommer. “Polymer brushes in explicit poor solvents studied using a new variant of the bond fluctuation model”. In: *J. Chem. Phys* 141 (2014), p. 104908.

[74] Anna Lappala, Saahil Mendiratta, and Eugene M. Terentjev. “Arrested spinodal decomposition in polymer brush collapsing in poor solvent”. In: *Macromolecules* 48.6 (2015), pp. 1894–1900.

[75] Blair Brettmann, Philip Pincus, and Matthew Tirrell. “Lateral Structure Formation in Polyelectrolyte Brushes Induced by Multivalent Ions”. In: *Macromolecules* 50.3 (2017), pp. 1225–1235.

[76] Carmen Bartic and Gustaaf Borghs. “Organic thin-film transistors as transducers for (bio) analytical applications”. In: *Analytical and Bioanalytical Chemistry* 384.2 (2006), pp. 354–365.

Appendix A

Python Analysis Code for Characteristic Length Scale

```
"""
Created on Thu Jan 10 10:32:34 2019
@author: T Trumpour
Last Edited: 2019-05-06
Program for processing of AFM images after being processed in gwyddion
"""
#-----------------------------------import packages---------------------------#
import glob
import numpy as np
import matplotlib.pyplot as plt
import scipy.signal as sp
from scipy.optimize import curve_fit
import fnmatch
from itertools import groupby
from operator import itemgetter
plt.rcParams.update({'font.size': 16})

#--------------------------functions----------------------------------#
def decay(x,a,h,c):
return np.log(a*(x**(-2*(1+h)))+c)  #logarithmic fitting function due to semilogy
axis
```

```
def FindMaxLength(lst):
maxList = max(lst, key = lambda i: len(list(i)))
return maxList

#----------------------process background capillary data-------------------#
nm_cubed=np.array([1e+027]*255, dtype='float64') #convert to m^3
nm=np.array([1e-009]*255, dtype='float64') #convert to m

for filename in glob.iglob ("C:\\Users\\tiana\\OneDrive\\Documents\\MSc\\Research\\Morp
with open(filename) as g:
x=np.array(list(zip(*[line.split()for line in g]))[0]) #first column of sheet
x=np.delete(x,0)  #delete the header
x=np.asarray(x,dtype='float64') #cast as type
with open(filename) as f:
y= np.array(list(zip(*[line.split() for line in f]))[1]) #second column of sheet
y=np.delete(y,0)  #delete the header
y=np.asarray(y, dtype='float64') #cast as type

power=np.multiply(y,nm_cubed) #power spectrum in m
inv_spatial=np.multiply(x,nm) #inverse spatial length in m
length=np.divide((2*np.pi),inv_spatial) #inverse length calculation
popt,pcov=curve_fit(decay,inv_spatial,np.log(power),bounds=((-np.inf,-1,-10),(np.inf,np
#fit a curve to the background data

#-------------------process solvent data-----------------------------------#
for files in glob.iglob("C:\\Users\\tiana\\OneDrive\\Documents\\MSc\\Research\\Morpholo
with open(files) as h:
v=np.array(list(zip(*[line.split()for line in h]))[0]) #first column of sheet
v=np.delete(v,0)  #delete the header
v=np.asarray(v,dtype='float64') #cast as type
with open(files) as j:
w= np.array(list(zip(*[line.split() for line in j]))[1]) #second column of sheet
w=np.delete(w,0)  #delete the header
w=np.asarray(w, dtype='float64') #cast as type

if fnmatch.fnmatch(files,"*_2um.txt"):  #change this each time for different
scan sizes
power_data=np.multiply(w,nm_cubed) #power spectrum in m
```

```
power_smoothed=sp.savgol_filter(power_data,41,4) #smooth power spectrum with
savgol filter
inv_spatial_data=np.multiply(v,nm) #inverse spatial length in m
length=np.divide((2*np.pi),inv_spatial_data) #inverse length calculation

indexing=np.where(np.log(power_smoothed) > decay(inv_spatial_data,popt[0],popt[1],popt
#find indices where data is greater than background value
lengths=[]
for k,g in groupby(enumerate(indexing), lambda i: i[0]-i[1]):
lengths.append((list(map(itemgetter(1),g))))
peak_indices=FindMaxLength(lengths)
outputPower=power_smoothed[peak_indices[0]:peak_indices[-1]]
outputDecay=decay(inv_spatial_data[peak_indices[0]:peak_indices[-1]],popt[0],popt[1],po
outputSpatial=inv_spatial_data[peak_indices[0]:peak_indices[-1]]
sub_data_y=np.log(outputPower)-outputDecay #subtract background from data
peak=np.argmax(sub_data_y) #find main peak
length_scale=(2*np.pi)/outputSpatial[peak] #calculate length scale from PSD
length_new=(2*np.pi)/outputSpatial
print(files,length_scale)

##----------------------naming for figures--------------------------------#
name=str(files)
portion=name[-21:-4]
newname=portion.replace('_'," ")
newname1=newname.replace("\\",'')
newname2=newname1.replace('rK','')
newname3=newname2.replace('eK','')
newname4=newname3.replace('K','')
newname5=newname4.replace('re','')

###--------------------------figures-----------------------------------#
plt.figure()
plt.rcParams["font.family"] = "serif"
plt.subplots_adjust(left=None, bottom=None, right=None, top=None, wspace=None,
hspace=0.4)
plt.suptitle(newname5)   #cut this to be proper title
plt.subplot(2,2,1)
plt.title('No Solvent with Background Fit')
```

```
plt.xlabel('Inverse Wavelength (1/nm)')
plt.ylabel('Power (nm^3)')
plt.plot(inv_spatial,np.log(power), color='b', label='Untreated Data', linewidth=2.5)
plt.plot(inv_spatial,decay(inv_spatial,popt[0],popt[1],popt[2]),'--', color='g',
label='Background Fit', linewidth=2.5)
plt.legend(loc='upper right')

plt.subplot(2,2,2)
plt.title('Solvent with Smoothing and Background Fit')
plt.xlabel('Inverse Wavelength (1/nm)')
plt.ylabel('Power (nm^3)')
plt.plot(inv_spatial_data,np.log(power_data), color='b', label='Treated Data',
linewidth=2.5)
plt.plot(inv_spatial_data,np.log(power_smoothed), color='k', label='Smoothed
Treated Data', linewidth=2.5)
plt.plot(inv_spatial,decay(inv_spatial,popt[0],popt[1],popt[2]), '--',color='g',
label='Background Fit', linewidth=2.5)
plt.legend(loc='upper right')

plt.subplot(2,2,3)
plt.title('Background Subtraction with Wavelength Peak')
plt.xlabel('Inverse Wavelength (1/nm)')
plt.ylabel ('Power (nm^3)')
plt.plot(outputSpatial,np.log(sub_data_y), color='k', label = 'Subtracted Treated
Data', linewidth=2.5)
plt.plot(outputSpatial[peak],np.log(sub_data_y[peak]),'x',color='r', markersize='12',
label= '2pi/Wavelength Peak')
plt.legend(loc='lower left')

plt.subplot(2,2,4)
plt.title('Background Subtraction with Length Scale')
plt.xlabel('Length Scale (nm)')
plt.ylabel('Power (nm^3)')
plt.loglog(length_new, sub_data_y, color='k', label = 'Subtracted Treated Data',
linewidth=2.5 )
plt.plot(length_new[peak],sub_data_y[peak],'x', color='r', markersize='12',
label= 'Length Peak')
plt.legend(loc='lower left')
```

```
plt.get_current_fig_manager().window.showMaximized()
plt.show()
plt.pause(0.1)
```